

Time-dependent boundary conditions with lead-sample Coulomb correlations: Application to classical and quantum nanoscale electron device simulators

G. Albareda, H. López, X. Cartoixà, J. Suñé, and X. Oriols*

Departament d'Enginyeria Electrònica, Universitat Autònoma de Barcelona, 08193 Bellaterra, Spain

(Received 28 March 2010; revised manuscript received 1 June 2010; published 2 August 2010)

Standard boundary conditions (BCs) for electron-transport simulators are based on specifying the value of the scalar potential (or the electric field) and the charge density at the borders of the simulation box. Due to the computational burden associated to quantum or atomistic descriptions, the use of small simulation boxes that exclude the leads is a mandatory requirement in modern nanoscale simulators. However, if the leads (where screening takes place) are excluded, standard BCs become inaccurate. In this work, we develop analytical expressions for the charge density, the electric field, and the scalar potential along the leads and reservoirs. From these expressions, we present a (time-dependent) BCs algorithm that transfers the specification of the BCs at the boundaries of the simulation box to a deeper position inside the reservoirs. Numerical solutions of the time-dependent Boltzmann equation with our algorithm using large (reservoir, leads, and sample) and small (sample alone) simulation boxes are compared, showing an excellent agreement even at (far from equilibrium) high bias conditions. Numerical results demonstrating the limitations of standard BCs for small simulation boxes are presented. Finally, time-dependent simulations of a resonant tunneling diode (using a quantum trajectory-based simulator) are presented, emphasizing the ability of this BCs algorithm to ensure overall charge neutrality in simulation boxes much smaller than the total lead-sample-lead length. This BCs algorithm requires a minimum computational effort and it can be applied to study dc, ac, and current or voltage fluctuations in nanoscale devices.

DOI: [10.1103/PhysRevB.82.085301](https://doi.org/10.1103/PhysRevB.82.085301)

PACS number(s): 85.30.-z, 41.20.Cv, 02.70.-c, 73.40.-c

I. INTRODUCTION

In order to correctly model the dc and/or ac conductance of nanoscale systems, one has to ensure “overall charge neutrality” and “current conservation.”^{1,2} The implementation of such requirements into modern nanoscale electron simulators demands some kind of reasonable approximation for the Coulomb interaction.

On one hand, the importance of overall charge neutrality (i.e., that the total charge in the whole device is zero) in nanoscale ballistic devices was clarified by the work of Landauer, Büttiker, and co-workers³ on the “two-terminal” and the “four-terminal” conductance of ballistic devices. The well-known standard textbook expression of the dc (zero-temperature) conductance through a tunneling obstacle is known as the two-terminal equation because it is defined as the current divided by the voltage drop sufficiently far from the obstacle. However, the original formulation of the conductance proposed by Landauer^{4,5} in 1957 was known as the four-terminal conductance because its experimental validation needs two additional voltage probes to measure the voltage drop close to the tunneling obstacle. The presence of resistances in the leads⁶ explains the difference between both expressions. The ultimate origin of such resistances is the requirement of overall charge neutrality that transforms unbalanced charges in the leads into a voltage drop there, via the Poisson (Gauss) equation. See Appendix A for a qualitative discussion of such lead resistances.

On the other hand, the “current conservation” (i.e., the total current computed on a surface in the simulation box is equal to the total current measured on a surface of an ammeter located far from the sample) is a necessary requirement for the prediction of ac conductances. The explicit consider-

ation of the displacement current, i.e., the time-dependent variations in the electric field, assures that the total (conduction plus displacement) current density is a divergenceless vector. Important theoretical contributions were done by Büttiker and co-workers for predicting ac properties of mesoscopic systems within a frequency-dependent scattering matrix formalism, in weakly nonlinear regimes taking into account overall charge neutrality and current conservation.^{1,7-12}

In general, modern electron-transport simulators do include reasonable approximations for the Coulomb interactions that can guarantee the accomplishment of the overall-charge-neutrality requirement. In addition, those simulators that are developed within a time-dependent or frequency-dependent framework can also assure the current conservation requirement. However, the powerful treatment of quantum and atomistic effects can only be applied to a very limited number of degrees of freedom.¹³ In fact, due to computational restrictions, a small simulation box is a mandatory requirement in many modern simulators. Here, the adjective small means that the leads are directly excluded from the simulation box. Neglecting the leads implies serious difficulties for the achievement of overall charge neutrality in the simulation box because the unbalanced charge in the leads is not considered. In addition, a possible inaccuracy in the computation of the overall charge neutrality affects our ability to treat the time-dependent Coulomb correlation among electrons and, therefore, the requirement of current conservation. In conclusion, due to computational difficulties, modern electron-transport simulators have to be implemented in small simulation boxes that imply important difficulties for providing dc or ac conductances of nanoscale devices because they neglect the lead-sample Coulomb correlation. An

exception to this conclusion appears in nanoscale devices with metallic leads that imply screening lengths of few Angstroms.^{14,15} However, many other scenarios with highly doped polysilicon leads or modern junctionless devices¹⁶ have screening length on the order of few nanometers. In addition, in all scenarios with far-from equilibrium conditions (with high bias), the screening length in the leads have to be complemented by the presence of a depletion length there.

In principle, the problem of excluding the leads from the simulation box, while retaining the lead-sample Coulomb correlation, could be solvable by providing adequate boundary conditions (BCs) on each of the “open” borders of the simulation box.¹⁷ In the literature, there are many different and successful BCs (Refs. 18–39) for describing nanoscale electron devices with simulation boxes large enough to include the leads. However, BCs found in the literature are not directly applicable for small simulation boxes. This is the main motivation of this work. Before presenting our BCs proposal, let us describe the standard BCs found in the literature for nanoscale electron device simulators. They are based on specifying two conditions at each of the borders of the simulation box:

(i) “*Border_charge_BC*s.” The charge density inside the simulation box depends on the electrons injected from its borders. Therefore, any BCs algorithm for electron devices has to include information on the charge density at the borders as an additional BCs assumption.

(ii) “*Border_potential_BC*s.” The value of the scalar potential (or electric field) on the borders of the simulation box has to be specified. This condition is a direct consequence of the uniqueness theorem for the Poisson equation¹⁷ which ensures that these values are enough to completely determine the solution of Poisson equation, when the charge inside the simulation domain is perfectly determined.

In many cases, the electrons injected through the boundaries depend, somehow, on the scalar potential determined by the “*border_potential_BC*s” (and a fixed electrochemical potential). Therefore, a coupled system of the two BCs appears.

Elaborated semiclassical electron-transport simulators solve the time-dependent Boltzmann equation by means of the Monte Carlo (MC) technique. In particular, most of them fix the potential at the borders of the box equal to the external bias and assume an *ad hoc* modification of the injection rate to achieve local charge neutrality.^{18–26} Some works do also include analytically the series resistances of a large reservoir²⁷ which can be considered an improvement over the previous “*border_potential_BC*s.” Other MC simulators consider Neumann BCs (i.e., a fixed zero electric field for “*border_potential_BC*s”).²⁸ In principle, there are no computational difficulties in applying the semiclassical MC technique in large (≈ 50 – 100 nm) simulation boxes. Nevertheless, the possibility of using smaller boxes will be very welcomed for some intensive time-consuming simulations. For example, to repeat multiple ($\sim 100\,000$) simulations to obtain statistical information about the macroscopic role of some uncertain microscopic parameter (such as impurity positions);²⁹ to simulate real three-dimensional (3D) solutions of the Poisson equation (involving matrix inversions of

~ 2 – 3000 nodes),³⁰ to compute (not only average values, but) current or voltage fluctuations that need very large simulation times (with $\sim 10^5$ and 10^6 time steps) to obtain reasonable estimators,^{21–23} to go beyond mean-field approximations,³⁰ etc.

The development of electron-transport simulators with the explicit consideration of the wave nature of electrons implies an important increase in the computational burden. The use of the external bias as the Dirichlet BCs (“*border_potential_BC*s”) was quite usual^{31,32} in the simulation of ballistic electron devices such as the resonant tunneling diode (RTD). The “*border_charge_BC*s” was directly specified from the energy difference between the fixed scalar potential and the fixed electrochemical potential. In 1989, Pötz³³ was one of the first in emphasizing the importance of flexible BCs at the borders of the simulation boxes of RTD to ensure local charge neutrality. Recently, more elaborated quantum-mechanical simulators are being used based on the self-consistent solution of the nonequilibrium Green’s functions and Poisson equation pioneered by Datta.^{34–39} They use either Dirichlet-type BCs (Refs. 34 and 35) or Neumann BCs (Refs. 36–39) for the “*border_potential_BC*s.” Again, the “*border_charge_BC*s” condition was indirectly determined from a fixed electrochemical potential and a fixed or floating scalar potential. All these BCs algorithms are very successful because they are implemented into simulation boxes large enough to explicitly include the leads. However, such algorithms are basically developed for static scenarios within a mean-field treatment of the Coulomb interaction. Its extension to time-dependent scenarios or the inclusion of correlations beyond the mean-field approximation has many computational difficulties that will certainly benefit from the possibility of using smaller simulation boxes.

As mentioned in the initial paragraphs, the extension of such quantum-transport to time-dependent scenarios is a complicated issue that requires not only overall charge neutrality but also current conservation. Büttiker and co-workers were the first to study quantum ac conductances with both requirements. They applied different many-body approximations (a simple one potential per conductor,⁷ a Thomas-Fermi screening potential,⁸ Hartree-type approximations,⁹ a treatment of the electron-electron interactions on the level of a Hartree-Fock approach,¹⁰ and also a generalization of the scattering matrix to deal with a Coulomb blockade system¹¹) to provide self-consistent theories for the ac conductance of mesoscopic systems. As a relevant example of their deep understanding of time-dependent mesoscopic scenarios, they predicted the value of the resistance in a quantum RC (single electronic mode) circuit,¹² which has been recently experimentally confirmed.⁴⁰ However, the practical implementation of the Büttiker theory for ac conductance in real RTD [with two-dimensional (2D) or 3D treatments] has many computational difficulties because of the use of large simulation boxes that have to include the leads explicitly (see Refs. 41 and 42).

Finally, there are even more computational difficulties in using large simulation boxes to include the leads in the so-called “first-principles” electron-transport simulators because of the huge demand of computational resources for their atomistic description. One strategy of such first-principles

simulators^{14,15} is based on dividing the whole system in three regions (left lead, sample,⁶ and right lead) and solving them separately. Once the (Hartree) potentials at the leads are known, the solution of the potentials in the sample is obtained by imposing that the Hartree potential in the simulation box matches those in the leads at equilibrium. If an external bias is applied, they shift the scalar (Hartree) potential between each lead exactly equal to this applied bias considering a negligible voltage drop in the leads. This specifies “*border_potential_BC*s” assuming that the screening effects are shorter than few tens of Angstroms. However, as discussed in the introduction, such small screening lengths are only applicable for metallic leads close to equilibrium but invalid in most practical scenarios of electron devices. In addition, although it is not explicitly explained, the “*border_charge_BC*s” is determined from standard Fermi (zero-temperature) statistics that depend on the energetic separation between a fixed electrochemical potential and the bottom of the conduction band. Whether or not such condition implies local or overall charge neutrality in the whole structure is not considered. Another approach is the one developed by Di Ventra, Lang, and co-workers^{43–47} where a specific discussion of the “*border_charge_BC*s” to ensure overall charge neutrality inside the simulation box is considered. Assuming a jellium model for the leads and letting the bottom of the conduction band to move relative to the electrochemical potential, they are able to assure overall charge neutrality in their lead-sample-lead simulation box. Their algorithm imposes an energy separation between a fixed electrochemical potential and a floating bottom of the conduction band (i.e., “*border_potential_BC*s”) that provides local charge neutrality deep inside the leads. In addition, an *ad hoc* (δ) charge density has to be included into the sample-lead interface (without any clear physical justification), in order to make compatible their local and global charge-neutrality requirements. Once more, the algorithm is numerically applied to systems with leads and small screening length. The modification of the previous BCs toward explicit time-dependent density-functional models, where the requirement of current conservation will be necessary, is starting to be developed.^{46–49}

In summary, the strategies mentioned above for specifying the BCs at the borders of the simulation box are similar for classical or quantum simulators. However, as we will show numerically in Sec. IV B, none of these BCs can be applied in simulation boxes that explicitly exclude the leads. The successful educated guesses applied in large simulation boxes become inapplicable in small simulation boxes. Neither the charge density, nor the electric field nor the scalar potential has easily predictable values at the borders of the sample. In addition, the energy distribution of electrons close to the active region can be very different from its thermal energy distribution deep inside the reservoirs. Therefore, the value of the electrochemical potential deep inside has no direct relevance close to the sample. The key point of our BCs is that we will not impose any of the previous requirements at the borders of the sample. We will obtain analytical expressions for the charge density, electric field, and scalar potential in the leads. Such analytical expression will allow us to transfer the BC deep inside the reservoirs into informa-

tion of charge density, electric field, and scalar potential at the sample borders. This BCs algorithm requires a minimum computational effort and it can be implemented in either quantum or classical time-dependent simulators with large or small simulation boxes, for dc and ac conditions, and even for the study of current (or voltage) fluctuations.

The structure of this paper is as follow. After this introduction, in Sec. II, we discuss some preliminary issues that will be used for the description of the BCs. In particular, we first discuss the time-dependent overall charge neutrality requirements, modeled through the dielectric relaxation time. Later, we present a simple parametric analytical expression of the impedance of the leads. Finally, we present a time-dependent degenerate injection model to control the charge density at the borders of the simulation box. In Sec. III, we develop our original time-dependent BCs algorithm taking into account all the ingredients discussed in Sec. II. In Sec. IV, we test our BCs algorithm with semiclassical MC simulations of a nanoscale silicon resistor with large and small simulation boxes. The excellent agreement between both sets of simulations (without any fitting parameter) confirms the merit and accuracy of our BCs algorithm. We also present a numerical simulation for a (quantum) double barrier RTD to show the importance of the BCs discussed here. The conclusions are presented in Sec. V. There are two additional appendixes. First, we summarize the enlightening work of Landauer and Büttiker about the role of the lead resistances in the overall charge neutrality. Second, we discuss the limits of the quasistatic electromagnetic approximation to justify the exclusive use of a scalar potential in time-dependent scenarios.

II. PRELIMINARY ISSUES

The original motivation of this work was the development of a BCs algorithm with an appropriate treatment of the lead-sample correlation for a general-purpose many-particle quantum-trajectory electron-transport simulator, previously developed by one of the authors.⁵⁰ From a computational point of view, such a quantum-trajectory algorithm (with Coulomb and exchange interactions) can only be implemented in small simulation boxes. Before presenting our algorithm, we develop some preliminary expressions that will be later used in Sec. III.

A. Time-dependent overall charge neutrality in nanoscale electron devices

We are interested in developing our BCs algorithm in a time-dependent framework because of the following two reasons. First, because it will be applicable not only to obtain dc (zero-frequency) results, but also to ac (high-frequency) ones. Second, because it is known that the lead-sample correlations are better treated with time-dependent BCs conditions that allow the exchange of energy between the leads and the sample.

In order to impose a time-dependent condition for the solutions of the charge density $\rho(\vec{r}, t)$, the electric field $\vec{E}(\vec{r}, t)$, and the scalar potential $V(\vec{r}, t)$, we start by integrating

the local continuity equation [i.e., the charge conservation implicit in Maxwell's Eq. (B2)] in a large volume Ω , that includes the sample, the leads and the reservoirs

$$\frac{\partial}{\partial t} \int_{\Omega} \rho(\vec{r}, t) \cdot dv + \int_S \vec{J}_C(\vec{r}, t) \cdot d\vec{s} = 0. \quad (1)$$

The volume Ω is limited by the surface S . We assume that the particle current $\vec{J}_C(\vec{r}, t)$ in Eq. (1) is parallel to all the subsurfaces of S , except in those open surfaces¹⁷ ($\vec{r}_S \in A_S$ in the source and $\vec{r}_D \in A_D$ in the drain reservoirs), which are perpendicular to the transport direction

$$\frac{\partial}{\partial t} \int_{\Omega} \rho(\vec{r}, t) \cdot dv + \int_{A_S} \vec{J}_C(\vec{r}_S, t) \cdot d\vec{s}_S + \int_{A_D} \vec{J}_C(\vec{r}_D, t) \cdot d\vec{s}_D = 0. \quad (2)$$

Next, we assume that the current density and the electric field at the surfaces $\vec{r}_S \in A_S$ and $\vec{r}_D \in A_D$, deep inside the reservoirs, are related by the Ohm law⁵¹ (no Ohmic assumption is imposed in this volume Ω). Thus

$$\int_{A_{S/D}} \vec{J}_C(\vec{r}, t) \cdot d\vec{s} = \sigma \int_{A_{S/D}} \vec{E}(\vec{r}, t) \cdot d\vec{s} \quad (3)$$

being σ the reservoir (frequency-independent) conductivity. The use of expression (3) imposes an important limitation on the frequency validity of our BCs algorithm. For example, the Drude's deduction of Ohm's law requires times which are larger than the inelastic scattering time. We can rewrite Eqs. (2) and (3) as

$$\frac{\partial}{\partial t} \int_{\Omega} \rho(\vec{r}, t) \cdot dv + \sigma [E_S^C(t) + E_D^C(t)] = 0, \quad (4)$$

where we have defined $E_S^C(t) = -\int_{A_S} \vec{E}(\vec{r}_S, t) \cdot d\vec{s}_S$ and $E_D^C(t) = \int_{A_D} \vec{E}(\vec{r}_D, t) \cdot d\vec{s}_D$. See Fig. 1 for the explicit location of $E_S^C(t)$ and $E_D^C(t)$, deep inside the reservoir. The next step is the integration of the Gauss equation [Eq. (B4) in Appendix B] in the same volume

$$\int_{\Omega} \rho(\vec{r}, t) \cdot dv - \int_S \vec{D}(\vec{r}, t) \cdot d\vec{s} = 0, \quad (5)$$

where $\vec{D}(\vec{r}, t) = \varepsilon(\vec{r}) \cdot \vec{E}(\vec{r}, t)$ is the electric displacement field and $\varepsilon(\vec{r})$ the (frequency-independent) dielectric constant. Again, we assume that $\vec{D}(\vec{r}, t)$ is very small at all surfaces except at those at the source and drain. Therefore

$$\int_{\Omega} \rho(\vec{r}, t) \cdot dv - \varepsilon [E_S^C(t) + E_D^C(t)] = 0 \quad (6)$$

with $\varepsilon = \varepsilon(\vec{r}_d) = \varepsilon(\vec{r}_s)$. Combining expressions (4) and (6), we obtain

$$\frac{\partial}{\partial t} \int_{\Omega} \rho(\vec{r}, t) \cdot dv = -\frac{\sigma}{\varepsilon} \int_{\Omega} \rho(\vec{r}, t) \cdot dv. \quad (7)$$

Expression (7) provides the time evolution of the total charge $Q(t) = \int_{\Omega} \rho(\vec{r}, t) \cdot dv$ in the whole system. Its solution is

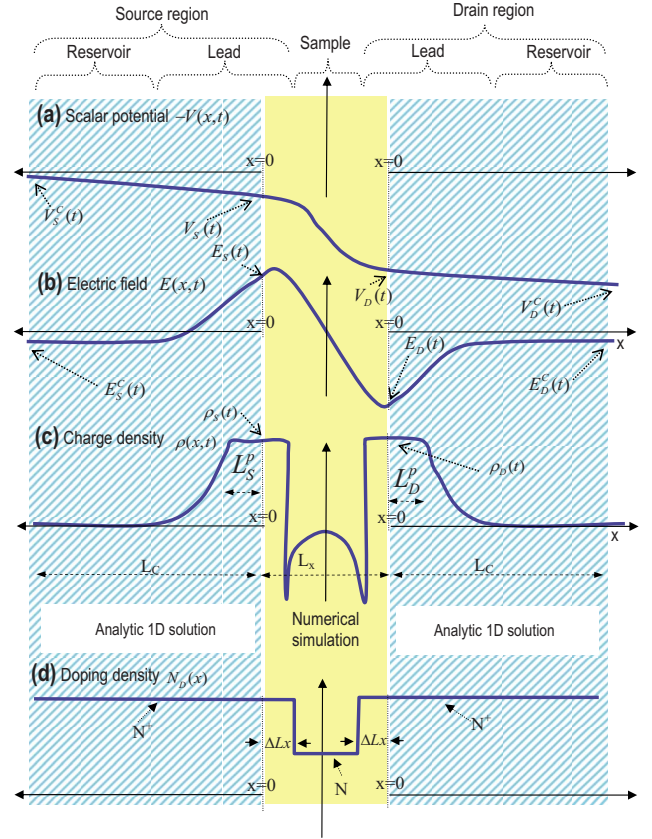


FIG. 1. (Color online) Definition of the variables used in the BCs algorithm and schematic representation of the (a) scalar potential, (b) electric field, (c) total charge density, and (d) doping density. An analytical parametric 1D solution is deduced in the (blue) dashed region while a numerical 3D solution is obtained in the (yellow) solid central region that we define as the simulation box. A part ΔLx of the highly doping leads is included into the simulation box in order to account for complex phenomena that can appear at the interface.

$$Q(t) = Q(t_0) \cdot \exp\left(-\frac{t-t_0}{\tau_c}\right) \quad (8)$$

with the dielectric relaxation time (sometimes called Maxwell relaxation time) being defined as

$$\tau_c = \varepsilon / \sigma. \quad (9)$$

As expected, the meaning of expression (8) is that the total charge inside the system tends to zero in periods of time related to the dielectric relaxation time. Identically, from Eqs. (4) and (6), we see that

$$E_S^C(t) - E_D^C(t) = [E_S^C(t_0) - E_D^C(t_0)] \cdot \exp\left(-\frac{t-t_0}{\tau_c}\right) \quad (10)$$

this meaning that the electric field tends to be the same deep inside both reservoirs. Finally, we know that the time-averaged electric field deep inside the reservoir tends to the Drude value $E_{SID}^{drift}(t)$. Therefore, one possible solution of Eq. (10) with the additional requirement $E_{SID}^C(t) \rightarrow E_{SID}^{drift}(t)$ when $t \gg \tau_c$ is

$$E_S^C(t) - E_S^{drift}(t) = [E_S^C(t_0) - E_S^{drift}(t_0)] \cdot \exp\left(-\frac{t-t_0}{\tau_c}\right) \quad (11)$$

and

$$E_D^{drift}(t) - E_D^C(t) = [E_D^{drift}(t)(t_0) - E_D^C(t_0)] \cdot \exp\left(-\frac{t-t_0}{\tau_c}\right). \quad (12)$$

When imposing $E_S^{drift}(t) = E_D^{drift}(t)$, we recover Eq. (10) by summing Eqs. (11) and (12). The frequency limitation of expressions (11) and (12) is ultimately determined by the assumption that the parameters σ and ε are constant (time independent and frequency independent). Therefore, the dielectric relaxation time used in expressions (11) and (12) cannot be shorter than the interval of time needed for making reasonable the assumption that σ and ε are constants.

B. Analytical spatial-dependent charge density, electric field, and scalar potential in the leads

In order to evaluate the total charge in expression (8) or to apply expressions (11) and (12), we need to know the charge densities or the electric fields deep inside the leads. Since we are interested in not explicitly simulating the leads, we look for analytical expressions. Nonlinear screening theory is important but a general analytical solution to the Poisson equation does not exist. Therefore, we will have to make some simplifying assumptions. We will use the schemes depicted in Fig. 1 to explain our analytical solution in the leads and the assumed simplifications. Throughout this paper, we will assume a two-terminal device, source and drain, to explain our BCs algorithm. In any case, it can be straightforwardly adapted to multiterminal systems with an arbitrary number of open boundaries.⁵²

First, we assume that all expressions in the leads depend only on the variable x along the transport direction but are independent on the lateral directions y and z so that a one-dimensional (1D) scheme in the leads and reservoirs is appropriate. In order to develop simpler analytical expressions we consider one specific negative x axis, $(-\infty, 0]$, for the source and another positive, $[0, +\infty)$, for the drain with different origins. The point $x=0$ is located at the interface between the numerical solution in the simulation box and the analytical solution in the lead (see Fig. 1). Let us notice that a small part of the lead is explicitly included into the simulation box (see the length ΔLx in Fig. 1). The exact length ΔLx depends on a trade-off between computational limitations and accuracy to treat complex effects in the interfaces (such as the presence of quasibound states in the accumulation well⁵³ or the Friedel oscillations⁵⁴).

Second, we assume that the electron charge distribution in the leads can be reasonably described by standard textbook⁵¹ expressions and that charge density due to ionized impurities is uniformly distributed in the leads and reservoirs. Therefore, we write the Poisson equation as

$$\frac{\varepsilon}{q} \frac{\partial^2 \Delta Ec(x,t)}{\partial x^2} = \rho(x,t) = qN_D \left\{ 1 - \exp\left[\frac{\Delta Ec(x,t)}{k_B \cdot \Theta}\right] \right\}, \quad (13)$$

where N_D is the uniform doping density, $\Delta Ec(x,t) = Ec(x,t) - Ec$ is the offset of the bottom of the conduction band measured from its average value deep inside the reservoir $Ec = Ec(x_{S/D}, t)$, Θ the absolute temperature, and k_B the Boltzmann constant. The bottom of the conduction band $Ec(x,t)$ and the scalar potential are related by $Ec(x,t) = -qV(x,t)$ (more complex screening theories can also be adapted to our BCs algorithm as far as they provide analytical solutions in the leads^{54,55}). We assume the standard Debye approximation⁵¹ $|\Delta Ec(x,t)| \leq k_B \cdot \Theta$ to solve the Poisson Eq. (13). Then, under a first-order Taylor expansion, we obtain $\rho(x,t) \approx \frac{qN_D \Delta Ec(x,t)}{k_B \cdot \Theta}$. Then, the solution of Eq. (13) in the source lead $-L_C \leq x \leq 0$ is

$$\rho(x,t) = \rho_S(t) \exp\left(\frac{x+L_S^p}{l}\right), \quad (14)$$

where we have assumed $\rho(x,t) = 0$ when $x \rightarrow -\infty$ because of the screening. We have defined $\rho_S(t) = \rho(-L_S^p, t)$ as the (surface-averaged) electron density at $x = -L_S^p$ (see Fig. 1). We can identify the parameter l as the Debye length⁵¹

$$l = \sqrt{\frac{\varepsilon \cdot k_B \cdot \Theta}{q^2 N_D}}. \quad (15)$$

Identically, the solution in the drain lead $0 \leq x \leq L_C$ is

$$\rho(x,t) = \rho_D(t) \exp\left(-\frac{x-L_D^p}{l}\right). \quad (16)$$

For simplicity, we assume equal doping densities and screening lengths in the drain and source leads. Expressions (14) and (16) are only valid for small applied bias, i.e., close to equilibrium conditions. However, large bias can drive the device far from equilibrium. For such conditions, it is quite usual that one lead suffers accumulation of electrons while the other suffers depletion. In the depleted regions, there are no electrons that can participate on the screening of positive charge, therefore, the screening length has to be complemented with an additional depletion length. See a schematic plot in Fig. 1(c). Then, a reasonable expression for the charge density at the source is

$$\rho(x,t) = \begin{cases} \rho_S(t) \exp\left(\frac{x+L_S^p}{l}\right) & -L_C \leq x \leq -L_S^p \\ \rho_S(t) & -L_S^p \leq x \leq 0, \end{cases} \quad (17)$$

where L_S^p is the depletion length of the source lead indicated in Fig. 1. Identically, the charge density in the drain lead is

$$\rho(x,t) = \begin{cases} \rho_D(t) \exp\left(-\frac{x-L_D^p}{l}\right) & L_D^p \leq x \leq L_C \\ \rho_D(t) & 0 \leq x \leq L_D^p. \end{cases} \quad (18)$$

By applying the Gauss Eq. (B4), from Eq. (17) we can determine the electric field along the source lead and the source reservoir

$$E(x,t) = \begin{cases} E_S^C(t) + \frac{\rho_S(t)l}{\varepsilon} \exp\left(\frac{x+L_S^p}{l}\right) & -L_C \leq x \leq -L_S^p \\ E_S^C(t) + \frac{\rho_S(t)(l+L_S^p)}{\varepsilon} + \frac{\rho_S(t)x}{\varepsilon} & -L_S^p \leq x \leq 0. \end{cases} \quad (19)$$

We use the field flux $E_S^C(t)$ as a boundary condition at $x=-L_C$ that reflects the expected series resistance of the reservoir. The other term in the right-hand side of Eq. (19) is due to the nonhomogeneity of the charge distribution in

the lead-sample region. Identically, in the drain lead, we obtain

$$E(x,t) = \begin{cases} E_D^C(t) - \frac{\rho_D(t)l}{\varepsilon} \exp\left(\frac{-x+L_D^p}{l}\right) & L_D^p \leq x \leq L_C \\ E_D^C(t) - \frac{\rho_D(t)(l+L_D^p)}{\varepsilon} + \frac{\rho_D(t)x}{\varepsilon} & 0 \leq x \leq L_D^p. \end{cases} \quad (20)$$

Finally, the definition of the scalar potential in the source leads is given by the spatial integration of expression (19) as

$$V(x,t) = \begin{cases} V_S^C(t) - E_S^C(t)(x+L_C) - \frac{\rho_S(t)l^2}{\varepsilon} \exp\left(\frac{x+L_S^p}{l}\right) & -L_C \leq x \leq -L_S^p \\ V_S^C(t) - E_S^C(t)(x+L_C) - \frac{\rho_S(t)(x+L_S^p)^2}{2 \cdot \varepsilon} - \frac{\rho_S(t)l(l+L_S^p+x)}{\varepsilon} & -L_S^p \leq x \leq 0 \end{cases} \quad (21)$$

and integration of Eq. (20) in the drain

$$V(x,t) = \begin{cases} V_D^C(t) + E_D^C(t)(-x+L_C) - \frac{\rho_D(t)l^2}{\varepsilon} \exp\left(\frac{-x+L_D^p}{l}\right) & L_D^p \leq x \leq L_C \\ V_D^C(t) + E_D^C(t)(-x+L_C) - \frac{\rho_D(t)(-x+L_S^p)^2}{2 \cdot \varepsilon} - \frac{\rho_D(t)l(l+L_S^p-x)}{\varepsilon} & 0 \leq x \leq L_D^p. \end{cases} \quad (22)$$

Apart from the frequency restrictions mentioned in Sec. II A, the validity of expressions (17)–(22) is limited to frequencies lower than the plasma frequency in the leads. In addition, when large bias conditions are considered, the presence of hot carriers (with high velocities) in the leads will modify the (quasiequilibrium) screening length found in Eq. (15). This effect will provide a limitation of our BCs model for very high bias.

C. Electron injection model for a zero-external impedance system

As discussed above, the previous expressions depend on the charge density at the source $\rho_S(t)=\rho(0,t)$ and drain $\rho_D(t)=\rho(0,t)$ borders. Electrons leaving the sample affect these charge densities but they cannot be controlled. On the contrary, we can model electrons entering into the simulation boxes through the injection of electrons from its borders. Let us discuss how to define such injection of electrons.

A time-dependent degenerate (i.e., taking into account the Pauli exclusion principle) injection model for electron devices has been presented by one of the authors in Ref. 56 under the assumption that the sample is part of a circuit with zero-external impedance. In this simplified scenario, the voltage drop in the sample can be viewed as a fixed nonfluctuating quantity equal to the external bias. In this section, we will present a brief summary of such injection model and its ability to determine either the average value of the current or

its time-dependent fluctuations. Then, in Sec. III, we will discuss how this injection model can be adapted to situations with arbitrary external impedance.

The rate and randomness of the injection of electrons into the sample can be modeled through the following binomial probability $P(k_x, N, \tau)$ defined in Ref. 56

$$P(k_x, N, \tau) = \frac{M_\tau!}{N! \cdot (M_\tau - N)!} f_{S/D}(E)^N [1 - f_{S/D}(E)]^{M_\tau - N}. \quad (23)$$

This expression defines the probability that N electrons with wave vectors in the range $k_x \in [k_{ox}, k_{ox} + \Delta k_x]$ are injected into the sample during the time interval τ . The parameter M_τ is the number of attempts of injecting electrons during the previous time interval τ , defined as a number that rounds the quotient τ/t_0 to the nearest natural number toward zero. The number of injected electrons can be $N=1, 2, \dots, \leq M_\tau$. The time t_0 is the minimum temporal separation between the injection of two electrons into the particular cell phase-space cell $k_x \in [k_{ox}, k_{ox} + \Delta k_x]$ and $x \in [x_o, x_o + \Delta x]$. For a 1D system, the value of t_0 can be easily estimated. The number of electrons n_{1D} in the particular phase space cell $\Delta k_x \cdot \Delta x$ is $n_{1D} = 2 \cdot \Delta k_x \cdot \Delta x / (2\pi)$ where we consider a factor 2 for spin degeneracy.⁵⁷ These electrons have been injected into Δx during the time interval Δt defined as the time needed for electrons with velocity $v_x = \Delta x / \Delta t = \hbar k_x / m_t$ to travel a distance Δx . Therefore, the minimum temporal separation, t_0 ,

between the injection of two electrons into the previous particular cell is Δt divided by the maximum number n_{1D} of electrons

$$t_0(k_x)|_{1D} = \frac{\Delta t}{n_{1D}} = \left(\frac{1}{\pi} \frac{\hbar k_x}{m_t} \Delta k_x \right)^{-1}. \quad (24A)$$

The practical application of such definition of t_0 requires a mesh with a small step Δk_x on all possible values of k_x . Identically, for a 2D and 3D system, we obtain

$$t_0(y, k_x, k_y)|_{2D} = \frac{\Delta t}{n_{2D}} = \left(\frac{1}{2\pi^2} \frac{\hbar k_x}{m_t} \Delta y \Delta k_x \Delta k_y \right)^{-1}, \quad (24B)$$

$$t_0(y, z, k_x, k_y, k_z)|_{3D} = \frac{\Delta t}{n_{3D}} = \left(\frac{1}{4\pi^3} \frac{\hbar k_x}{m_t} \Delta y \Delta z \Delta k_x \Delta k_y \Delta k_z \right)^{-1}. \quad (24C)$$

On the other hand, the function $f_S(E)$ that appears in Eq. (23) determines the probability that a state with kinetic energy E measured from the bottom of the conduction band $-qV_S(t)$ is occupied by an electron that will effectively enter into the simulation box. In particular, we assume that such probability is determined by half of the Fermi distribution [$E = E(\vec{k})$ with $k_x > 0$,] as:

$$f_S(E) = \frac{1}{1 + \exp \left[\frac{E - F_S^{inj}(t) + qV_S(t)}{k_B \cdot \Theta} \right]} \quad (25)$$

where the electron wave vector \vec{k} is related to the kinetic energy by the appropriate energy-dispersion relationship $E(\vec{k})$. The term $F_S^{inj}(t)$ is defined here as the source injecting energy level and it determines how to increase the rate of injection of electrons while respecting the Pauli restriction. This restriction implies that two electrons with identical velocity have to be injected with a temporal separation equal or larger than t_0 . We avoid the name electrochemical potential for such energy $F_S^{inj}(t)$ because Eq. (25) does not refer to all (source) electrons but only to those with $k_x > 0$. In addition, close to the active region, the electron distribution for $k_x < 0$ will be quite unpredictable (see insets in Fig. 18 in Appendix A). We reserve the name electrochemical potential to the thermalized energy distribution deep inside the reservoirs, at $x = \mp L_C$. Here, $F_S^{inj}(t)$ is just a parameter that controls the rate of injection of electrons at the border of the simulation box to ensure overall charge neutrality. Equivalently, the electrons injected from the drain have an energy distribution determined by [$E = E(\vec{k})$ with $k_x < 0$] as:

$$f_D(E) = \frac{1}{1 + \exp \left[\frac{E - F_D^{inj}(t) + qV_D(t)}{k_B \cdot \Theta} \right]} \quad (26)$$

with $F_D^{inj}(t)$ the drain injecting energy level. We will later use the parameters $F_S^{inj}(t)$ and $F_D^{inj}(t)$ to indirectly increase/decrease the charge density $\rho_{S/D}(t)$ at the lead-sample interface, at each time step of the simulation.

It is very instructive to understand the Binomial distribution of the injection process, expression (23), as a consequence of the discreteness of the electron charge. For a particular cell, at zero temperature, we inject an electron every interval of time t_0 . The average current per cell is $-q/t_0$. At room temperature, the average current is lower, $-q \cdot f(E)/t_0$, because of the uncertainty in the occupation. However, it is not possible to inject a fractional charge $-qf(E)$ into the system at each interval of time t_0 (i.e., the electron charge is indivisible). Therefore, at each interval of time t_0 , either we inject the full charge, $-q$ (if the state is occupied), or we do not inject charge (if the state is empty) according to the probability $f(E)$.

As a simple test of our injection model in zero-external impedance circuits, we compute analytically the current and its fluctuations (i.e., the noise) for a one-subband ballistic 1D system. According to the zero-external impedance, we assume that $V_S(t)$ and $V_D(t)$ in Eqs. (25) and (26) are fixed by the time-independent external bias. We assume a transmittance equal to unity. For such conditions, all injected electrons are finally transmitted (i.e., injection probability and the transmitting probability are identical) and there are well-known analytical results in the literature for both, average current and noise.^{1,58,59}

The average current $\langle I \rangle$ is an experimental measure of the charged transmitted through the system during a long time interval. For our ballistic system, the charge transmitted through the source is just the charge injected. Therefore

$$\langle I \rangle = - \lim_{\tau \rightarrow \infty} q \sum_{k_x} \frac{E_N[\tau, k_x]}{\tau}. \quad (27)$$

The average number $E_N[\tau, k_x]$ of injected particles during the time interval τ is computed from the probability $P(k_x, N, \tau)$

$$E_N[\tau, k_x] = \sum_{N=0}^{N=\infty} P(k_x, N, \tau) N. \quad (28)$$

As we mentioned before, we divide the whole phase space into cells with a small Δk_x so that all electrons in the cell have roughly the same energy. The average number of injected particles with wave vector k_x during the time τ can be computed from Eq. (28) as $E_N[\tau, k_x] = f_S(E) \cdot \tau / t_0(k_x)$ for each cell of the source injection. Previous expression is just the mean value of the Binomial distribution in Eq. (23), where $f_S(E)$ is defined by expression (25). From Eq. (27), the average current of each k_x -phase space cell can be computed as $\langle I \rangle^{k_x} = -q f_S(E) / t_0(k_x)$. The sum over all phase-space cells with $k_x > 0$, $\langle I \rangle = \sum_{k_x} \langle I \rangle^{k_x}$, does exactly reproduce the Landauer average current. The drain current is computed equivalently. The total current is the source component minus the drain component

$$\langle I \rangle = -\frac{2q}{h} \int_0^\infty [f_S(E) - f_D(E)] dE, \quad (29)$$

where we have used $dE \approx \hbar^2 k_x \cdot \Delta k_x / m_t$ and $1/t_0(k_x) = \hbar k_x \cdot dk_x / (\pi \cdot m_t)$. This is just expressions (39) and (40) of Ref. 1 for a transmission coefficient equal to one. For low temperature [i.e., $f(E)=1$ for all injected electrons], we obtain the well-known Landauer conductance $G=2q^2/h$.

For ballistic devices, the one-side power spectral density of the current fluctuations at zero (low) frequency can be also obtained from probability in Eq. (23) as

$$S_I(0) = \lim_{\tau \rightarrow \infty} 2q^2 \sum_{k_x} \frac{E_{N^2}[\tau, k_x] - (E_N[\tau, k_x])^2}{\tau}, \quad (30)$$

where we defined $E_{N^2}[\tau, k_x]$ as

$$E_{N^2}[\tau, k_x] = \sum_{N=0}^{N=\infty} P(k_x, N, \tau) N^2. \quad (31)$$

For the binomial distribution of expression (23), we obtain $E_{N^2}[\tau, k_x] - [E_N(\tau, k_x)]^2 = f_S(E)[1 - f_S(E)] \cdot \tau / t_0(k_x)$. Then, using Eq. (30), we found $S_I^{k_x}(0) = 2q^2 f_S(E)[1 - f_S(E)] / t_0(k_x)$ for the source injection. Identical results are obtained for the drain injection. Since there is no drain-source correlation in our simple ballistic model, the total power is the sum of both. After integration over all energies, we obtain

$$S_I(0) = \frac{4q^2}{h} \int_0^\infty \{f_S(E)[1 - f_S(E)] + f_D(E)[1 - f_D(E)]\} dE. \quad (32)$$

This expression does exactly reproduce Büttiker results for a system with transmission coefficient equal to one [see expression (61) in Ref. 58]. Expression (32) includes the thermal and the shot noise (i.e., it is valid both at equilibrium and far from equilibrium). Under equilibrium conditions, the previous result reproduces the Nyquist-Johnson thermal noise, as can be shown by introducing the identity $-k_B \Theta \cdot \partial f(E) / \partial E = f(E)[1 - f(E)]$ into the previous result.

In conclusion, the (time-dependent) injection model discussed here correctly accounts for the Pauli correlations among electrons when the active region is part of a circuit with zero-external impedance. In this case, the voltages applied to the sample can be viewed as a fixed nonfluctuating quantity and the noise properties are determined only by the Pauli correlations discussed above. In addition, when the sample is a part of a larger circuit (with nonzero-external impedances), the current fluctuations in the sample imply voltage fluctuations in the leads [through the time dependence of $V_S(t)$ and $V_D(t)$ in Eqs. (25) and (26)] that, in turn, imply fluctuations on the injecting probabilities into the sample [through expression (23)] and on the current in the sample [see expression (63) in Ref. 1]. These complicated correlations between sample and leads highlight the importance of the BCs algorithm mentioned here.

III. TIME-DEPENDENT BOUNDARY-CONDITIONS AT THE BORDERS OF THE SAMPLE FOR OVERALL CHARGE NEUTRALITY

A. General consideration

According to Fig. 1, we have to specify the values $V_S(t)$ and $V_D(t)$ for the “border_potential_BCs,” and $\rho_S(t)$ and $\rho_D(t)$ for the “border_charge_BCs.” In addition, in Sec. II B, we have derived analytical relationships between scalar potentials, electric fields, and charge densities at the borders of the simulation box, at $x=0$, and those values deep inside the reservoirs, at $x=\mp L_C$. We have to add the four additional unknowns $V_S^C(t)$, $V_D^C(t)$, $E_D^C(t)$, and $E_S^C(t)$. In total, for two-terminal models, we have eight unknowns. Hence, we need eight conditions to specify the BCs.

As we have explained in the introduction, and it will be numerically confirmed in Sec. IV, it is very difficult to provide an educated guess of the scalar potential, the electric field or the charge density at the borders of a small simulation box where leads are excluded. In addition, the electrochemical potential for thermal distributions becomes an ill-defined parameter for small simulation boxes. One can assume a well-known value of the electrochemical potential deep inside the reservoir. However, close to the active region, where the (far from equilibrium) momentum distribution can be quite arbitrary, the prediction of any value of the electrochemical potential for injected and reflected electrons is quite inappropriate.

Fortunately, the analytical results of Sec. II for the leads and reservoirs can be used to transfer the unknown “border_potential_BCs” and “border_charge_BCs” at the borders of the simulation box into simpler BCs deep inside the reservoirs. This is the key point of our BCs algorithm. In particular, the two new BCs that we will impose at $x=\mp L_C$ are:

(i) “Deep_drift_BCs.” We assume that the inelastic scattering mechanisms at, both, the source $x \leq -L_C$ and the drain $x \geq L_C$ reservoirs provides a quasiequilibrium position-independent thermal distribution of electrons (it is implicitly assumed that the contact length L_C is large enough so that inelastic scattering is relevant there). Such position-independent electron distribution is consistent with charge neutrality deduced in expressions (17) and (18), deep inside the reservoir, that implies a uniform electric field there. Then, according to the Ohm’s law mentioned in expression (3), we know that the electric fields tend to $E_{S/D}^C(t) \rightarrow E_{S/D}^{drift}(t)$ at the source and drain reservoir.

(ii) “Deep_potential_BCs.” We assume that electrochemical potentials can be defined for the position-independent thermal distribution deep inside both reservoirs. We know that the applied bias coincides with the energy separation of the electrochemical potentials between the source and drain reservoirs. In addition, due to the position-independent electron distribution deep inside the reservoirs, we assume that the energy separation between the electrochemical potential and the bottom of the conduction band is perfectly known in the drain and source reservoirs. When equal doping is used in both contacts (as done in the numerical examples of this work), the energy separation between the bottoms of the

conduction bands at both reservoirs is equal to the difference of the external voltages. Hence, $V_S^C(t)=0$ and $V_D^C(t)=V_{external}(t)$.

These two conditions, “*deep_drift_BC*s” and “*deep_potential_BC*s” are quite reasonable for any electron device deep inside the reservoirs. In fact, we will show in Sec. III B that the numerical MC solution of the nonequilibrium Boltzmann equation in a large simulation box confirms the adequacy of these conditions in the reservoirs. Therefore, from the initial eight unknowns, we have the “*deep_drift_BC*s” and “*deep_potential_BC*s” considerations that provide four conditions (two for each border). However, we do still need four additional conditions in order to completely specify our BCs unknowns. Such conditions come from imposing, at the borders of the simulation box, the continuity between the analytical expression of the electric field (and the scalar potential) in the leads and the numerical values obtained inside the simulation box. Therefore, we will be able to determine the initial unknowns $V_S(t)$, $V_D(t)$, $\rho_S(t)$, and $\rho_D(t)$ in the borders of the simulation box, by imposing four conditions deep inside the reservoir and imposing continuous profiles. The value of the $E_{S/D}^{drift}(t)$ is not a parameter because it is imposed by the conduction current, via the Ohm’s law. As discussed in Sec. II A, imposing equal electric fields deep inside the reservoirs guarantees the overall-charge-neutrality requirement.

Finally, we have to comment on the time dependence of our algorithm. On one hand, most of the expressions developed in Sec. II have some frequency restrictions. In Appendix B, we have also discussed the frequency limitations related to assuming that only the scalar potential is necessary to describe time-dependent nanoscale scenarios. Our BCs algorithm is valid for frequencies lower or equal than the lowest-frequency restriction mentioned above. We will refer to such frequency limit as the, f^{qs} , which will be considered in next section.

B. Practical implementation of the boundary conditions in classical or quantum time-dependent simulators

In Fig. 2, we represent schematically the flux diagram of the BCs algorithm presented in this paper. After initializing all variables and functions to predetermined values and moving particles (or solving wave-equation time evolution), we arrive at the specific BCs algorithm. We know the old values of $V_S(t)$, $V_D(t)$, $\rho_S(t)$, and $\rho_D(t)$ at time t . The BCs algorithm will provide their new values at time $t=t+\Delta t$. We have divided the algorithm into five different steps that we will describe in detail below:

Step (1) evaluation of the charge density at the sample (inside) boundary. The first step is the evaluation of the charge density at the boundaries of the sample at time t . This will be computed in the spatial cell closer to the border but still inside the simulation box (see ΔLx in Fig. 1). Since we describe a one-dimensional version of the BCs algorithm, we will need a surface integration of such magnitudes that we refer to as the instantaneous charge densities $\rho_{S/D}^{ins}(t')$. As mentioned before, due to frequency restrictions of the algorithm, what we will finally compute is a running average

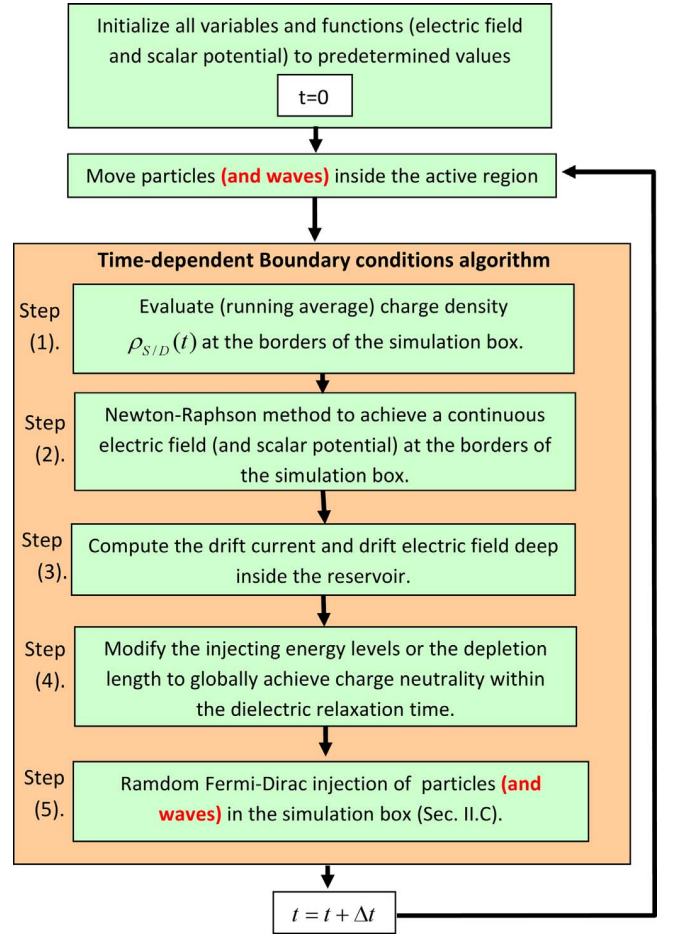


FIG. 2. (Color online) Schematic representation of our (time-dependent) BCs algorithm coupled to a particle-based electron (classic and quantum) transport simulator.

$$\rho_{S/D}(t) = \frac{1}{T^{qs}} \cdot \int_{t-T^{qs}}^t \rho_{S/D}^{ins}(t') \cdot dt' \quad (33)$$

with the temporal interval T^{qs} equal to the integer N^{qs} multiplied by the simulation time step, $T^{qs} = N^{qs} \cdot \Delta t \approx 1/f^{qs}$. Let us notice that we just calculate the charge density at time t , not at time $t+\Delta t$.

Step (2)—imposing continuity of the electric field and the scalar potential at the sample-lead interface by means of a Newton-Raphson method. As mentioned in the previous section, the electric field and the scalar potential have to be continuous at both lead-sample interfaces. In one hand, the electric field, at the $x=0$ and the electric field at $x=-L_C$, of the source lead, are related from expression (19) as

$$E_S^C(t+\Delta t) = E_S(t+\Delta t) - \frac{\rho_S(t)[l + L_S^p(t)]}{\epsilon}, \quad (34)$$

where we have defined $E_S(t+\Delta t) = E(0, t+\Delta t)$. Here, we assume $\rho_{S/D}(t+\Delta t) \approx \rho_{S/D}(t)$ and $L_{S/D}^p(t+\Delta t) \approx L_{S/D}^p(t)$. We will later relax these assumptions. Identically, from Eq. (20), we define in the drain

$$E_D^C(t + \Delta t) = E_D(t + \Delta t) + \frac{\rho_D(t)[l + L_D^p(t)]}{\varepsilon}. \quad (35)$$

In addition, from Eq. (21), we obtain

$$V_S(t + \Delta t) = V_S^C(t + \Delta t) - E_S^C(t + \Delta t)L_C - \frac{\rho_S(t)[l + L_S^p(t)]^2}{2\varepsilon} - \frac{\rho_S(t)l^2}{2\varepsilon} \quad (36)$$

and from Eq. (22)

$$V_D(t + \Delta t) = V_D^C(t + \Delta t) + E_D^C(t + \Delta t)L_C - \frac{\rho_D(t)[l + L_D^p(t)]^2}{2\varepsilon} - \frac{\rho_D(t)l^2}{2\varepsilon}. \quad (37)$$

As mentioned before, we fix the value $V_S^C(t + \Delta t) = 0$ and $V_D^C(t + \Delta t) = V_{external}(t + \Delta t)$. We also know the charge density $\rho_S(t)$ and $\rho_D(t)$ from “step 1.” We will use $E_S^C(t + \Delta t)$ and $E_D^C(t + \Delta t)$ to find the continuous solution of the electric field according to the procedure explained in the next paragraph. Later, in “step 4,” we will relate the new parameters of $E_S^C(t + \Delta t)$ and $E_D^C(t + \Delta t)$ to new values of $\rho_S(t + \Delta t)$ and $\rho_D(t + \Delta t)$.

We will follow a Newton-Raphson method to find the best parameters $E_S^C(t + \Delta t)$ and $E_D^C(t + \Delta t)$ that provide continuity of the electric field at the borders of the simulation box. We use expressions (34) and (35) to determine $E_S(t + \Delta t)$ and $E_D(t + \Delta t)$, and Eqs. (36) and (37) for $V_S(t + \Delta t)$ and $V_D(t + \Delta t)$. Then, we apply these new voltages on the source and drain surfaces of the 3D simulation box and solve the 3D Poisson equation there. Next, we compute the electric field at the spatial step closer to the borders but still inside the 3D simulation box. We made a surface integral to transform the electric field in the surface of the simulation box into a 1D parameter. In order to obtain a continuous shape of the electric field in the whole system we repeat the previous sequence by slightly modifying the values of $E_S^C(t + \Delta t) \pm \delta E$ and/or $E_D^C(t + \Delta t) \pm \delta E$ until we find new values $V_S(t + \Delta t)$ in Eq. (36) and $V_D(t + \Delta t)$ in Eq. (37) so that the analytical and numerical electric fields at the borders of the simulation boxes coincide. Such a loop will provide a continuous analytical-numerical coupling for the electric field and, as a consequence, will also assure the continuity of the scalar potential. In summary, in this step 2, we determine the new values $V_S(t + \Delta t)$ and $V_D(t + \Delta t)$.

Step-(3) calculation of the drift electric field at $x = \mp L_C$. The $J_{S/D}^{drift}(t)$ is computed inside the sample from the number of electrons crossing the source (or drain) surfaces. In addition, the value $J_{drift}(t)$ is time averaged as described in expression (33).

$$J_{S/D}^{drift}(t) = \frac{1}{T^{bc}} \cdot \int_{t-T^{bc}}^t J_{S/D}^{drift-ins}(t') dt', \quad (38)$$

where $J_{S/D}^{drift-ins}(t')$ is the value computed at each time step. Finally, from the Ohm's law of expression (3) we will compute the average drift electric fields deep inside the reservoirs at $x = \mp L_C$. Let us notice that we just calculate the drift electric field at time t , not at $t + \Delta t$.

Step 4—modification of the injecting energy levels and the depletion lengths. In step 2 we have already computed $E_S^C(t + \Delta t)$ and $E_D^C(t + \Delta t)$ as fitting parameters instead of $\rho_S(t + \Delta t)$ and $\rho_D(t + \Delta t)$. In this step, we will relate the modification of the electric fields deep inside the reservoir to the charge density at the borders of the simulation box. This two-step procedure is justified because we deal with a very small time step, which implies very small variations of all these parameters. From Eqs. (11) and (19), we can state a direct relationship that gives the value of the charge density required at the borders of the active region in the next time step

$$\rho_S(t + \Delta t) = \rho_S(t) + [E_S^C(t) - E_S^{drift}(t)] \frac{\varepsilon \cdot \Delta T}{[l + L_S^p(t)] \cdot \tau_c} \quad (39)$$

and from Eqs. (12) and (20)

$$\rho_D(t + \Delta t) = \rho_D(t) - [E_D^C(t) - E_S^{drift}(t)] \frac{\varepsilon \cdot \Delta T}{[l + L_D^p(t)] \cdot \tau_c}. \quad (40)$$

We have assumed the following simplification, $\exp[-(t-t_0)/\tau_c] \approx 1 - \Delta t/\tau_c$ with $\Delta t = t - t_0$ which is much smaller than τ_c , in expressions (11) and (12). Since we are only interested on relating $E_{S/D}^C(t)$ with $\rho_{S/D}(t + \Delta t)$, we have assumed that $E_{S/D}(t)$ and $L_{S/D}^p(t)$ in expressions (19) and (20) does not change with time.

Although Eqs. (39) and (40) together with the values $\rho_S(t)$ and $\rho_D(t)$ clearly define $\rho_S(t + \Delta t)$ and $\rho_D(t + \Delta t)$, we do not have a complete control on how to increase/decrease these values in our simulator. On the contrary, we only have the possibility of increasing/decreasing the injecting probability in Eq. (23) through the parameters $F_S^{inj}(t + \Delta t)$ and $F_D^{inj}(t + \Delta t)$ that appear in Eqs. (25) and (26). The exact relationship between the displacement of the injecting energy levels and the variation in the injected charge density in the simulation box boundaries is not trivial. We perform a pre-processing computation of the function $\rho^{inj}(F_{S,D}^{inj} + qV_{S,D})$ according to the injection model described in Sec. II C. Once such a relation has been established, we can determine exactly in which way the injecting energy levels have to be displaced.

As mentioned several times along this paper, there is a particular scenario that cannot be managed just by modifying the injecting energy levels. Far from equilibrium, at high applied bias, we can accumulate electrons as much as needed to decrease $\rho_S(t)$ in order to achieve overall charge neutrality. However, we cannot deplete electrons as much as possible in the sample-lead interface. Once we arrive at zero injected electrons, we cannot decrease this number any more. In such situations, the only way to decrease the negative charge is to enlarge the depleted (positive charge) region in the drain [see Fig. 1(c)]. The same depletion procedure could be needed in the source for a negative bias. From Eqs. (11) and (19), if we consider $\rho_S(t)$ fixed but $L_S^p(t)$ variable, we obtain in the source

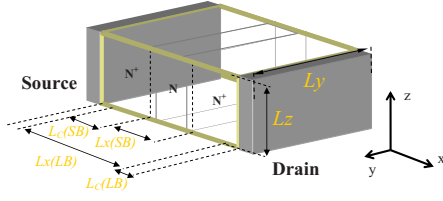


FIG. 3. (Color online) Schematic representation of the N^+NN^+ structure.

$$L_S^p(t + \Delta t) = L_S^p(t) + [E_S^C(t) - E_S^{drift}(t)] \frac{\varepsilon \cdot \Delta t}{\rho_S(t) \cdot \tau_c} \quad (41)$$

and, identically from Eqs. (12) and (20), we obtain in the drain

$$L_D^p(t + \Delta t) = L_D^p(t) - [E_D^C(t) - E_D^{drift}(t)] \frac{\varepsilon \cdot \Delta t}{\rho_D(t) \cdot \tau_c}. \quad (42)$$

At this point, we have determined the evolution of the injection energy levels $F_{S/D}^{inj}(t + \Delta t)$ and the depletion lengths $L_{S/D}^p(t + \Delta t)$.

Step 5-electron injection. Finally, according to the new values of the scalar potential $V_{S/D}(t + \Delta t)$ (step 2) and the injecting energy levels $F_{S/D}^{inj}(t + \Delta t)$ (step 4) at the boundaries of the simulation box, a new injecting process is performed according to expressions developed in Sec. II C. This is the last step of the BCs algorithm before the simulator can go back to moving the particles (and waves) as shown in the flux diagram of Fig. 2.

These five steps of the BCs algorithm are repeated for each time step. The time step is so small, $\Delta t \sim fs$, so that very small variations in all magnitudes are obtained. In turn, these very small variations justify the approximations developed in the procedure explained above.

IV. NUMERICAL RESULTS

Now, we report the numerical results obtained by applying the previous BCs to classical and quantum (time-dependent) electron-transport simulators. All simulations are carried out at room temperature.

A. Testing of our boundary condition algorithm: Comparison between large and small simulation boxes

In this section, we consider the N^+NN^+ resistor depicted in Fig. 3 with two different simulation boxes. First, a large simulation box (LB), $L_x(LB) = 42$ nm, that includes the leads and reservoirs (N^+ region) plus the sample (N region). Second, a smaller simulation box (SB), $L_x(SB) = 8$ nm, that only includes the sample (N region) plus a small part, $\Delta L_x(SB)$, of the leads. See Fig. 3 and Table I. We will use the semiclassical MC simulator⁶⁰ of Ref. 30 that provides a detailed treatment of the Coulomb correlations among electrons inside the device. The use of the smaller simulation box certainly implies a considerable reduction in the computational burden. In particular, while the computational times related with the LB simulations imply approximately 1 day per bias

TABLE I. Parameters for the N^+NN^+ structure depicted on Fig. 3.

	Units	Symbol	Value
Lengths	(nm)	$L_x(LB)$	42
		$L_x(SB)$	8
		L_y	60
		L_z	60
		$L_C(LB)$	3
		$L_C(SB)$	20
Spatial step	(nm)	Δx	1
		Δy	60
		Δz	60
Relative permittivity		Air	1.0005
		Silicon	11.7514
Dielectric relaxation time	(sec.)	τ_c	1×10^{-13}
Silicon conductivity	$(\Omega \text{ m})^{-1}$	σ	2.5×10^5
Screening length	(nm)	l	0.95
Doping	(cm^{-3})	Channel N	Intrinsic
		Contact N^+	2×10^{19}
Simulation time	(sec.)	T	2×10^{-10}
Temporal step	(sec.)	Δt	2×10^{-16}

point in our computing tools because of the large number of particles simulated, its simulation with the SB decreases down to only 3 h.

Before comparing the SB and LB results, let us mention some details common to both sets of MC simulations.⁶⁰ We assume an effective-mass approximation.^{61,62} Electron transport in the “ x ” direction (from source to drain) takes place along a silicon (100) orientation channel, at room temperature. In particular, the electron mass is taken according to the six equivalent ellipsoidal constant energy valleys of the silicon band structure.^{63,64} The effective masses of the ellipsoids are $m_l^* = 0.9163m_0$ and $m_t^* = 0.1905m_0$ with m_0 the free electron mass. Finally, all simulations use a 3D finite-difference Poisson solver. Hence, the volumes Ω_{SB} (for the small box simulations) and Ω_{LB} (for the large box simulations) are divided into cells of spatial dimensions $\Delta X = 1$ nm, $\Delta Y = 60$ nm, and $\Delta Z = 60$ nm. See Table I for more details.

In Fig. 4, we have plotted (in dashed lines) the (time-averaged) self-consistent scalar potential for the LB. The results are obtained by applying our BCs algorithm explained in Sec. III for the large simulation box. In particular, we have used $L_C(LB) = 3$ nm so that, according to Fig. 1, the total length of the resistor is $2L_C(LB) + L_x(LB) = 48$ nm. Interestingly, the simulations reproduce a net charge equal to zero deep inside the reservoirs (see dashed line in Fig. 5) and a small uniform electric field proportional to the current, i.e., the drift value. The deep region of the reservoir can be modeled by a simpler series resistance confirming that our BCs algorithm can be perfectly used in large simulation boxes that include the leads. Then, our model provides the voltage drop due to a simpler (reservoir) series resistance. Another relevant issue of these LB results is that they provide a numerical justification of our “*deep_drift_BC*s” that

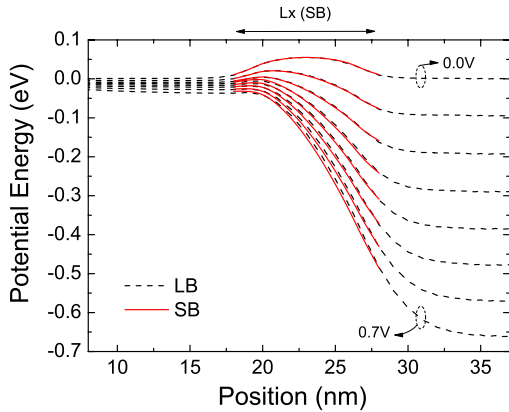


FIG. 4. (Color online) Potential-energy profile computed with our BCs algorithm for a large simulation box (dashed line) and for a small simulation box (solid lines).

we impose on our BCs algorithm deep inside the reservoir, i.e., $E_{SID}^C(t) \rightarrow E_{SID}^{drift}(t)$.

In Fig. 4, we have also plotted (in solid line) the (time-averaged) self-consistent scalar potential profiles obtained for the SB. In particular, we have used $L_c(\text{SB})=20$ nm so that, according to Fig. 1, the total length of the resistor in this second set of simulations, $2L_c(\text{SB})+L_x(\text{SB})=48$ nm, is identical to the first one. The agreement between both sets of simulations is excellent, even for large external bias. This highlights the accuracy of our BCs algorithm for simulation boxes of few nanometers and its ability for incorporating the Coulomb correlations among the electrons inside the sample (N region) and those located in the leads (N^+ region).

Figure 5 shows the charge density distribution along the N^+NN^+ structure for both sets of simulations. The agreement among the LB and SB curves is quite acceptable. Let us notice that charge density is the second derivative of the scalar potential distribution, and hence, the imperceptible discrepancies encountered in Fig. 4 are now magnified. The depletion region in the drain for large bias merits some special attention. An exponential shape describes reasonably well the charge density in the source lead, however, due to

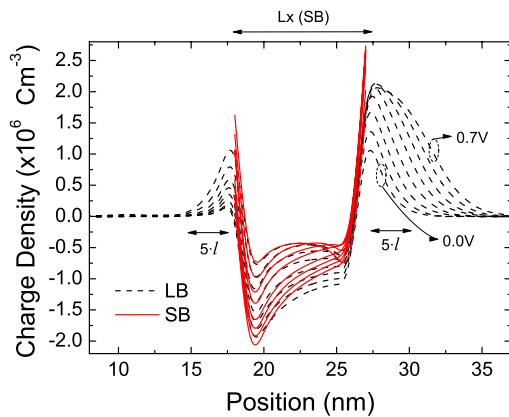


FIG. 5. (Color online) Charge-density profile computed with our BCs algorithm from a large simulation box (dashed line) and from a small simulation box (solid lines).

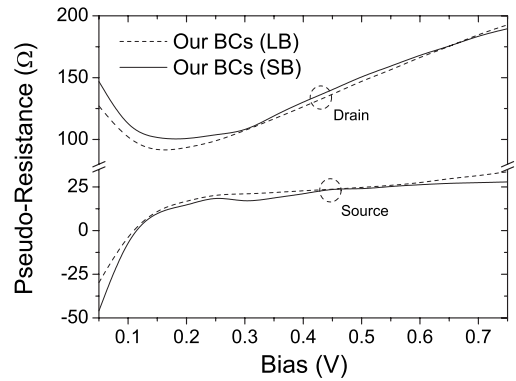


FIG. 6. Pseudoresistance of the reservoir plus lead computed from our BCs algorithm with a large simulation box (dashed lines) and with a small simulation box (solid lines).

the formation of a depletion region in the drain side, the charge there does not tend to zero within the five Debye lengths ($\sim 5l$). Due to the important voltage drop there, electrons coming from the drain reservoir are not able to reach the sample-lead interface and, therefore, they cannot screen the positive doping charge and a depletion region appears. The ability of dealing with depletion regions appearing in far from equilibrium scenarios represents an important landmark of our model.

There is an interesting explanation for the slight differences between the charge density in the LB and SB results. The semiclassical MC method⁶⁰ used in both sets of simulations only takes into account the Pauli exclusion principle in the electron injection process as described in Sec. II C. For example, in the source, it will not be possible to inject two electrons with identical positive velocity (wave vector) simultaneously. Our injecting process waits, at least, an interval of time t_0 before sending the second identical electron. However, once the electrons are inside the simulation box, the semiclassical MC technique does not impose any Pauli restriction on their dynamics so that, after a large enough time from their injection, two electrons can occupy the same position with the same velocity. In this sense, the momentum distribution at the boundaries (close to the active region) will be different when large or small simulation boxes are considered. When using small simulation boxes, the addition of electrons into the active region implies an increase in its energy because lower states are already occupied (i.e., the quantum capacitance). On the contrary, when using a large simulation box, the addition of electrons into the active region can come from identical energies. Interestingly, we can argue that (in the MC simulations) the small simulation box provides a better electron momentum close to the sample than that obtained with a large simulation box. The slight differences appearing in Fig. 5 might partially be explained by this effect.

Finally, Fig. 6 shows the contact plus lead pseudoresistances as a function of bias. They are defined directly as the voltage drop in the lead region divided by the (average) current flowing through the whole structure. From our definition, a negative value of the source resistance means that the potential energy deep inside the reservoir is lower than that

at the lead-sample interface (see, for example, the 0.0 V potential profile in Fig. 4). Obviously, the total (reservoir, leads plus sample) resistance in the whole electron device will be positive. We use the word “pseudo” to emphasize that such resistances cannot be directly associated to energy dissipation. As it can be observed, although the contact series resistances (related to the drift electric field deep inside the reservoir) are constant, the bias dependence of the resistance in the lead is far from trivial because it takes into account the complex electrostatic coupling of the leads and the sample described by expressions (36) and (37). This result shows that a constant resistance cannot account accurately for the Coulomb correlations between electrons in the active region and those in the leads.

In conclusion, in this section we have shown that our BCs provides an excellent description of the coulomb coupling between the sample and the leads. The (reservoir plus lead) resistance obtained from a LB simulation box is practically identical to that obtained from a SB simulation. The comparison of the current-voltage characteristic will be discussed in next section. Let us emphasize that our BCs algorithm is a parameter free algorithm. Only the external bias is necessary. Even the electric drift field is obtained from the numerical computation of the average conduction current. In next section, we show numerically the enormous difficulties that the standard BCs, applied to small simulation boxes that exclude the leads, have when trying to reproduce the previous set of results obtained with our algorithm.

B. Limitations of standard boundary condition algorithms for (small) simulation boxes that exclude the leads

In the present section, we simulate the same N^+NN^+ structure with the same MC technique and the same small simulation box (that excludes the leads) considered in the previous section. The only difference will be the consideration of two different BCs algorithms.

The first type of BCs, that we named *Dirichlet external bias*, uses the external bias as the BCs for the Poisson equation (“*border_potential_BC*s”) and the injection model de-

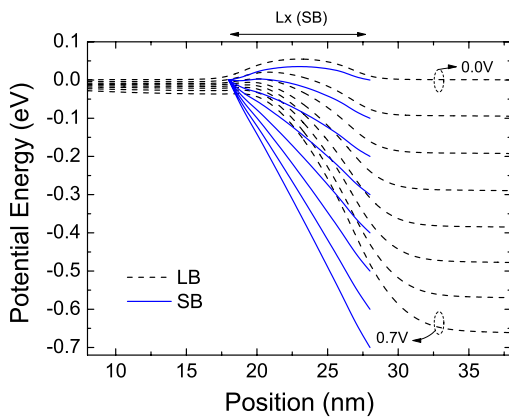


FIG. 7. (Color online) Scalar potential-energy profile computed in the large simulation box with our BCs algorithm (dashed lines) and that corresponding to the implementation of the Dirichlet external bias BCs in the small simulation box (solid lines).

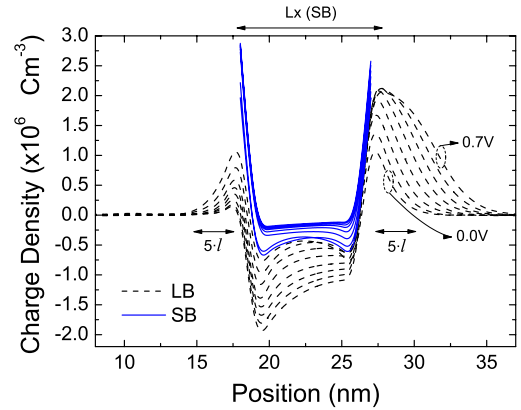


FIG. 8. (Color online) Charge-density profile computed in the large simulation box with our BCs algorithm (dashed lines) and that corresponding to the implementation of the Dirichlet external bias BCs in the small simulation box (solid lines).

scribed in Sec. II C with a fixed $F_{S/D}^{inj}(t)$ equal to the equilibrium electrochemical value (“*border_charge_BC*s”). Since such Dirichlet BCs consider zero-external impedance so that it can only be acceptable for large simulation boxes. Here, we explicitly demonstrate its limitations for small simulation boxes.

The second type of BCs, that we named *local charge neutrality*, is based on ensuring that the total charge is zero at the borders (“*border_charge_BC*s”). The *local charge neutrality* is achieved by moving the bottom of the conduction (border_scalar_BCs), while fixing $F_{S/D}^{inj}(t)$ equal to the equilibrium electrochemical value, to increase/decrease the charge at the border. This second type can be used in simulation boxes slightly smaller than the ones required by the previous BCs algorithm. In any case, although the assumption of local charge neutrality inside the leads (i.e., a few Debye lengths away from the lead-sample interface) is correct, it is not valid close to the active region as shown below.

The LB results depicted in Figs. 7–10 are the ones obtained in the previous subsection. The first type of BCs, the Dirichlet external bias implies a very restrictive constriction

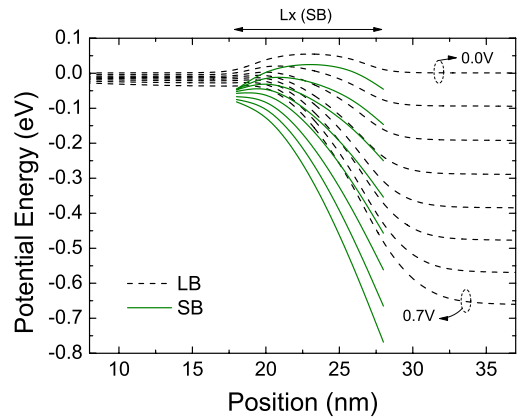


FIG. 9. (Color online) Scalar potential-energy profile computed in the large simulation box with our BCs algorithm (dashed lines) and that corresponding to the implementation of the local charge neutrality BCs model in the small simulation box (solid lines).

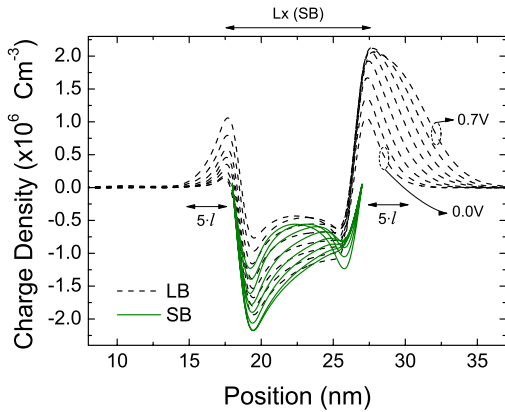


FIG. 10. (Color online) Charge-density profile computed in the large simulation box with our BCs algorithm (dashed lines) and with the local charge neutrality BCs model in the small simulation box (solid lines).

that neglects any correlation among the electrons inside and outside the active region. The scalar potential at the borders does not depend on the charge (accumulated or depleted) in the leads. As seen in Figs. 7 and 8, these limitations are obviously translated into a bad description of the conduction band and the charge density.

The second type of BCs in small simulation boxes, local charge neutrality, is plotted in Figs. 9 and 10. It cannot properly describe the (accumulated or depleted) charge at the N^+-N and $N-N^+$ interfaces. The charge density at those interfaces is always zero with these BCs (see Fig. 10). The condition of charge neutrality is reasonable deep inside the leads, but not close to the sample, where the excess/deficit of charge has not yet been screened. This second type of BCs is unable to properly describe the bottom of the conduction band depicted in Fig. 9.

The ultimate reason why none of the two previous BCs types are able to produce reasonable results is because they do not achieve the overall-charge-neutrality requirement discussed in the introduction. In Fig. 11, we demonstrate that a nonaccurate description of the lead-sample Coulomb corre-

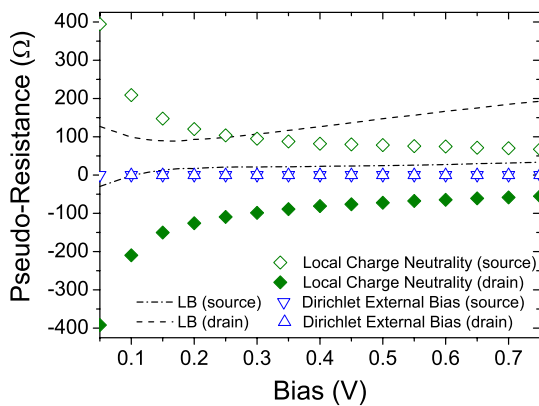


FIG. 11. (Color online) Pseudoresistance of the reservoir plus lead computed from our BCs model for the large simulation box (dashed lines) and from the Dirichlet external bias and local charge neutrality for the small simulation box (symbols).

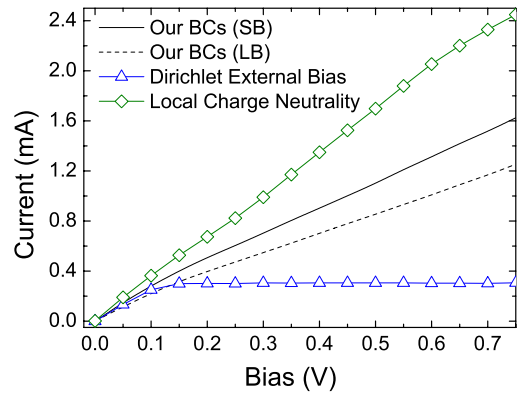


FIG. 12. (Color online) Current-voltage characteristics for the N^+NN^+ structure. The solid line corresponds to our BCs algorithm applied in the small box region. Open triangles correspond to Dirichlet external bias and open diamonds to local charge neutrality BCs. In dotted line we have plotted the I - V characteristic correspondent to our BCs applied in the large box including the leads.

lations cannot provides an accurate description of the (lead plus reservoir) pseudoresistance. The first type of BCs, Dirichlet external bias, gives a trivial and incorrect zero resistance. The second type, local charge neutrality, accounts for a nonlinear dependence of the resistances on the applied voltage that assumes some kind of electrostatic correlations between sample and leads. However, Fig. 11 shows that such correlations are clearly unphysical when small simulation boxes are considered.

Finally, in Fig. 12, we plot the characteristic current-voltage curves for the large and small simulation boxes computed by means of our BCs algorithm and those computed through the Dirichlet external bias and the local charge neutrality algorithms with small boxes. For very small voltages (close to equilibrium), all BCs gives similar results. However, for large voltages (far from equilibrium), the discrepancies among the different models are more than notable.

The Dirichlet external bias (open triangles) fixes not only the potential at the borders of the simulation box but also the electrochemical potentials there. This means that the injection of electrons in each side is independent of the rest of the system (and neglects the Coulomb correlations between electrons in the sample and the leads). Therefore, when the applied bias is enough to avoid that electrons coming from the drain contact reach the source, the current saturates. The local charge neutrality (open diamonds) wants to preserve charge neutrality, locally, in the lead border. As we increase the voltage, in the source border, the number of electrons reflected by the sample (with negative momentum) tends to decrease because most of source electrons are finally transmitted. In addition, the mean velocity of the carriers tends to increase in the active region implying a reduction in negative charge in the sample (while the positive charge remains constant). Therefore, when we increase the voltage, the source electron density at the source border tends to decrease and, consequently, the injection rate must increase to ensure local charge neutrality in the source border. This explains why the current saturates at a much larger voltage (not plotted in Fig. 12) than that obtained for the Dirichlet external voltage. A

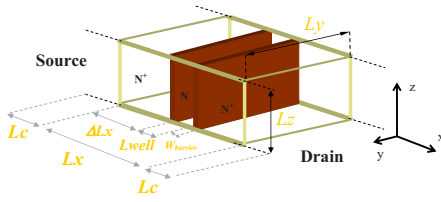


FIG. 13. (Color online) Schematic representation of the RTD.

similar explanation can be applied to understand the current-voltage obtained with our BCs model for a SB (solid lines). Again, the solution to obtain overall charge neutrality is to incorporate more and more electrons from the source but at slower rate. Certainly, our BCs model with a small box (solid line) is the one that provides currents closer to the LB results (dashed lines).

The small differences between the two curves obtained with our BCs for small and large boxes can be explained with the same arguments used to explain the differences in the charge density of Fig. 5. The MC method⁶⁰ used in both sets of simulations only takes into account the Pauli exclusion principle in the electron injection process at the boundaries of the simulation box, as described in Sec. II C. However, once the electrons are inside the simulation box, the semiclassical MC technique does not impose any (Pauli) restriction on their dynamics. When using small simulation boxes, the addition of electrons at the borders of the active region implies an increase in their (kinetic) energy because lower states are already occupied (this is not true for the LB because the injection is far from the borders of the active region). This means that the average velocity in the borders is slightly higher with the small simulation box than with the large one. Hence, as depicted in Fig. 12, the current computed with the SB is slightly higher than the LB current.

C. Application of our boundary condition algorithm for (time-dependent) quantum electron transport simulators

In this section, we provide an example of the implementation of our BCs algorithm into a time-dependent quantum simulator, where the need for small simulation boxes is still a more relevant computational requirement. In fact, it is not strange to find in the literature, atomistic structures with simulation boxes of few tens of Angstrom.^{14,15,45} In order to emphasize the relevance of taking into account the Coulomb correlations among the active region and the leads, we will compare the results obtained with our BCs model and those obtained through standard Dirichlet external bias at the borders of the simulation box. Contrarily to Sec. IV A, no comparison with a large simulation box (including the leads and reservoirs) is done because such simulation would be computationally inaccessible. This computational difficulty was, precisely, the initial motivation for this work.

As described in Fig. 13 and Table II, we consider an RTD consisting on two highly doped drain-source GaAs regions (the leads), two AlGaAs barriers, and a quantum well (the active region). Such structure is simulated with a quantum electron-transport simulator based on the algorithm dis-

TABLE II. Parameters for the RTD depicted on Fig. 13.

	Units	Symbol	Value
Lengths	(nm)	L_x	17.1
		L_y	48.6
		L_z	48.6
		ΔL_x	4.5
		L_C	6
		Equilibrium screening lengths	(nm)
Barrier dimensions	(eV)	High	0.6
Relative permittivity	(nm)	L_{well}	5.7
	(nm)	$W_{barrier}$	1.2
Spatial step (Poisson equation)		Air	1.0005
		GaAs	13.1800
Spatial step (Schrödinger equation)	(nm)	AlGaAs	11.7760
	(nm)	Δx	0.30
Spatial step (Schrödinger equation)	(nm)	Δy	8.1
		Δz	8.1
		Δx_S	0.3
Doping	(cm^{-3})	Channel N	Intrinsic
		Contact N^+	4.8×10^{18}
GaAs conductivity	$(\Omega \text{ m})^{-1}$	σ	1.5×10^5
Dielectric relaxation time	(sec.)	τ_c	5×10^{-14}
Simulation time	(sec.)	T	4×10^{-11}
Temporal step (Poisson equation)	(sec.)	Δt	8×10^{-16}
Temporal step (Schrödinger equation)	(sec.)	Δt_S	2×10^{-17}

cussed in Ref. 50, where it is demonstrated that the many-particle Schrödinger equation can be efficiently solved using quantum (Bohmian) trajectories computed from (time-dependent) single-particle Schrödinger equations. In this paper, we assume a constant effective mass $m=0.067m_o$, with m_o the electron free mass, along the whole structure that accounts for the interaction of free electrons with the periodic atomic structure under the Born-Oppenheimer approximation.⁶² In any case, the BCs algorithm presented in this paper can be straightforwardly adapted to a discrete description of the atom structure. Then, the analytical expressions of Sec. II B have to be matched to the Hartree potential of the simulation box. Transport takes place from source to drain direction. The lateral dimensions are $L_y=L_z=48.6$ nm. The practical quantum algorithm for the RTD implies solving numerically $N(t)$ time-dependent single-particle 1D Schrödinger equations⁵⁰ for the transport direction x . All Schrödinger equations are coupled to the Poisson equations with the BCs given by our algorithm. The number of electrons, $N(t)$, around 20–30, implies a computational time on the order of 1–2 days per bias point. In order to take into account the Friedel oscillations⁵⁴ and the formation of quasisubband states⁵³ in the leads, we extend the simulation box inside the leads a distance ΔL_x . More technical details about the computation of Bohmian trajectories can be found in Refs. 30 and 50 and Table II.

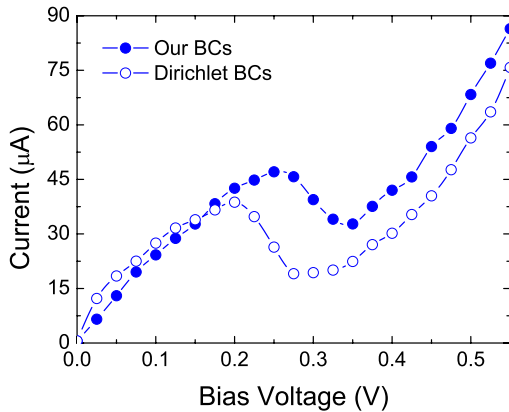


FIG. 14. (Color online) RTD Current-voltage characteristic taking according to our BCs algorithm (solid circles) and to a Dirichlet external bias BCs (open circles).

In Fig. 14, we present the current-voltage curves of the simulated RTD using our BCs algorithm (solid circles) and standard Dirichlet external bias BCs (open circles). As it can be observed, the differences between these two approaches appear not only in the magnitude of the current but also in the position of the resonant voltage. These differences are fully compatible with previous current-voltage simulations done with/without explicitly including the leads in the self-consistent simulation scheme.³³ The differences in Fig. 14 can be easily explained from the information depicted in Fig. 15.

In Fig. 15, we represent the (time-averaged) voltage drop $\Delta V_{S/D}$ of the scalar potential outside the simulation box defined as, $\Delta V_S = V_S^C - V_S$ in the source and $\Delta V_D = V_D - V_D^C$ in the drain regions. While Dirichlet BCs assume a zero-voltage drop outside the simulation box, our BCs algorithm predicts a nonlinear drop of the bottom of the conduction band at the borders of the simulation box. In particular, ΔV_D is higher than ΔV_S in magnitude and it is the main responsible of the displacement of the resonant voltage. As seen in the insets (a) and (b) of Fig. 15, our model predicts a drop of the scalar potential in the drain lead that maintains the resonant energy

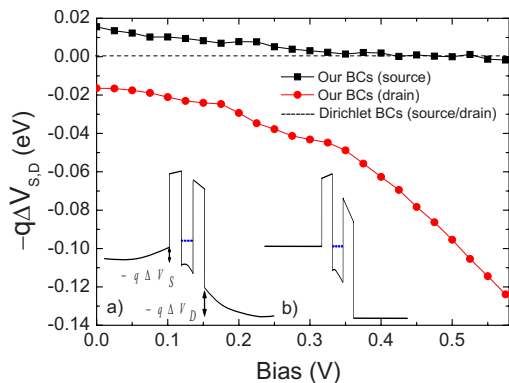


FIG. 15. (Color online) Potential-energy drop in the highly doped drain lead, $-q\Delta V_D$ (red circles), and in the source lead, $-q\Delta V_S$ (black squares). The insets represent a schematic representation of the potential energy profile at $V=0.2$ V using (a) our BCs algorithm and (b) the Dirichlet external bias approach.

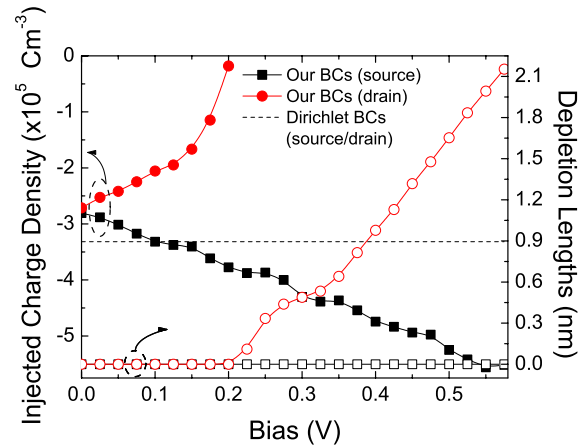


FIG. 16. (Color online) On the left axis: injecting charge density at the borders of the simulation box as a function of the applied bias. On the right axis: depletion lengths as a function of the applied bias. The dashed line represents the constant injected charge density obtained with external bias Dirichlet BCs.

level significantly above the bottom of the source conduction band at that particular 0.2 V bias (i.e., the resonant voltage for the Dirichlet external bias). As explained in Sec. III, the behavior of ΔV_D and ΔV_S is also coupled to the value of ρ_D and ρ_S . The latter, in turn, are the responsible of a higher source injection that explains the higher current when our BCs algorithm is used.

In Fig. 16, we discuss in detail the coupling between $\Delta V_{S/D}$ and $\rho_{S/D}$. First, let us notice that the BCs with a standard Dirichlet conditions equal to the external bias always injects electrons at the same rate because it does not allow neither a displacement of the bottom of the conduction band $V_{S/D}$ nor a movement of the injecting energy levels $F_{S,D}^{inj}$. Thus, the injecting probabilities of Eqs. (25) and (26) remain bias independent. On the contrary, our BCs algorithm does not fix any of the two parameters. We have only an indirect control on the values of $\rho_{S/D}$ because we can only increase/decrease the rate of injection into the simulation box by modifying the values $F_{S/D}^{inj}$ and $V_{S/D}$ [see expressions (25) and (26)]. As seen in Fig. 16, for bias below 0.15 V, the charge injected from the source border decreases while the charge injected from the drain increases with the bias. These injected charges and the potential profiles are consistent with the requirement of overall charge neutrality. In particular, the increase of the electrons injected from the source is the main reason why our algorithm predicts a larger current than the results obtained from a Dirichlet external bias. The situations changes when the external bias approaches 0.2 V. The probability of injecting electrons from the drain is very low so that any further decrease in the injecting energy level does not cause any variation in the charge density there. Therefore, the only way to decrease an excess of negative charge in the whole system, in order to achieve overall charge neutrality, is creating a depletion region at the drain side [see expression (42)]. For larger values of ΔV_D , the most relevant effect in the drain lead is not the screening of positive charge by electrons but the appearance of a depletion region. As discussed in Sec. IV A, this is an important contribution of

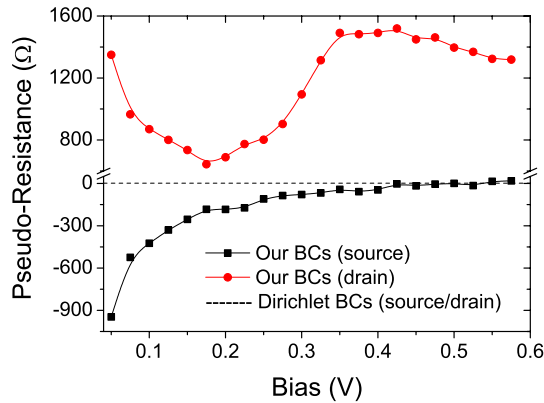


FIG. 17. (Color online) Pseudo-resistance of the RTD in the drain and source regions.

our BCs algorithm that allows us to satisfactorily simulate far from equilibrium conditions in small simulation boxes of electron devices.

Finally, in Fig. 17, we discuss the resulting pseudo- (reservoir plus lead) resistances. The external bias Dirichlet BCs predicts a zero effective resistance and our BCs algorithm describes a highly asymmetric and nonlinear behavior. Even more, the source pseudo-resistance takes negative values up to very high applied bias (the negative sign in the pseudo-resistance means a positive spatial derivative of the potential energy). In any case, obviously, the total (source, sample plus drain) resistance is positive. Importantly, the practical results of such lead resistances are quite different from the expressions (A1) and (A2) deduced in Appendix A, where a constant value of both resistances is predicted. In Appendix A, zero temperature is assumed while, here, we consider a room temperature and an energy-dependent density of states. In addition, in Appendix A, Poisson equation is substituted by some kind of linear “capacitor” that can be justified for small variations around equilibrium. However, here, we solve explicitly the Poisson equation and the charge is related not only to the number of electrons but also to its dynamics (fast electrons provide less charge than slow electrons).

In conclusion, in the results of the RTD with our BCs algorithm, we can guarantee that the profile of the charge density along the whole device (the reservoirs, the leads, and the sample) is compatible with the requirement of overall charge neutrality discussed in the introduction. In addition, we can also guarantee that the profiles of the electric field and scalar potential are self-consistent with the previous profile of the charge density. Even more, the requirement of overall charge neutrality is achieved in time intervals related with the relaxation dielectric time.

V. CONCLUSIONS

The Coulomb interaction among electrons introduces two fundamental requirements for the accurate simulation of electron devices. First, the screening of electrons implies that the total charge in the whole (reservoirs, leads plus sample⁶) device region is zero, i.e., overall charge neutrality. Second,

the total time-dependent current computed in a surface of the simulation box is equal to that measured by an ammeter far from the sample, i.e., current conservation.

Due to the computational burden associated to quantum and atomistic description of nanoscale structures, the explicit and accurate simulation of the lead-sample-lead region⁶ is not always possible. Therefore, quite often, a small simulation box that excludes the leads⁶ is a mandatory requirement in modern electron-transport simulators. This restriction on the box length is a serious problem for the requirement of overall charge neutrality because the total charge has to include the (accumulated/depleted) charge in the leads. In addition, the inaccuracy in achieving the overall-charge-neutrality requirement affects the computation of the time-dependent variations in the scalar potential (i.e., the electric field) and, thus, the requirement of current conservation.

As explained in the introduction, all BCs used in electron transport simulators are based on specifying the value of the scalar potential, or the electric field, at the borders of the simulation box (“border_potential_BCs”) and the charge density there (“border_charge_BCs”). However, it is very difficult to anticipate an educated guess for these magnitudes at the boundaries of a small simulation box that excludes the leads (see Sec. IV B). Alternatively, in Sec. II, we have developed analytical and time-dependent expressions for the charge density, the electric field, and the scalar potential along the leads and reservoirs. These analytical expressions take into account electron screening leading to accumulation and depletion regions in the leads. From these analytical expressions, we can transfer the assumptions about the BCs at the borders of a small simulation box into the simpler specifications of the BCs deep inside the reservoirs. This is the key point of our BCs algorithm. In particular, the two new BCs that we impose deep inside the reservoirs are, first, the electric field tends to a drift value $E_{S/D}^C(t) \rightarrow E_{S/D}^{drift}(t)$ (that we refer as “deep_drift_BCs”) and, second, the scalar potentials deep inside the reservoir is fixed by the external bias $V_S^C(t) = 0$ and $V_D^C(t) = V_{external}(t)$. In Sec. IV A, we have shown that these two new BCs conditions are perfectly supported from a numerical MC solution of the nonequilibrium Boltzmann equation in a large simulation box that includes the leads and reservoirs.

Our BCs algorithm requires a minimum computational effort and it can be implemented into either quantum or classical time-dependent simulators, for dc, ac, and current (or voltage) fluctuations. We have tested our BCs algorithm with semiclassical MC simulations of a nanoscale silicon resistor with large and small simulation boxes. As seen in Fig. 4, the excellent agreement between both sets of simulations confirms the accuracy of our BCs algorithm. Let us emphasize that no fitting parameter is used and that our BCs algorithm includes the trivial series resistance plus the complicated lead resistance (see Appendix A). We have also presented a numerical simulation for a (quantum) double barrier RTD to show the importance of the BCs discussed here. In particular, we have highlighted that our BCs algorithm is able to discuss far from equilibrium situations where depletion lengths in the leads have to be added to standard screening. Our BCs algorithm guarantees that the profile of the charge density along the whole device (not only along the simulation box

but the reservoirs, the leads, and the sample) is compatible with the requirement of overall charge neutrality and that the profiles of the electric field and scalar potential are self-consistent with the charge density along the whole device.

The numerical results presented in this paper deal with classical and quantum dc scenarios. However, our BCs algorithm can be equivalently applied to ac (time-dependent) scenarios up to a frequency f^{qs} (defined from the lowest-frequency restriction for the validity of expressions developed in Sec. II). The requirement of overall charge neutrality is achieved in time intervals related with the relaxation dielectric time of the device. Therefore, for time intervals lower than the inverse of f^{qs} , the temporal variations in the scalar potential (and the electric field) at the borders of the simulation box are physically meaningful because they are the reaction of the Coulomb interaction in the whole electron device system to temporal perturbation that deviates the device from its “state” compatible with overall charge neutrality. Such frequency-dependent correlations allows us to confidently compute the displacement current (i.e., time-dependent variations in the electric field inside) in the simulation box and assume that the total current computed there is equal to the value measured in an ammeter far from the simulation box, i.e., current conservation.

Identically, the frequency-dependent correlations included into our BCs algorithm, due to sample-lead Coulomb interaction, allow us to investigate the computation of (zero-frequency or high-frequency) current fluctuations beyond the standard external zero impedance assumption (i.e., most of the computations of current fluctuations in electron devices assume that the voltage applied in the simulation box is a nonfluctuating quantity). As discussed at the end of Sec. IV C, the intrinsic charge fluctuations are coupled to voltages fluctuations at the borders of the simulation boxes that, in turn, induce additional fluctuations of the injected charge (i.e., current) in a quite complicated self-consistent loop. Studies of these topics are in progress.

ACKNOWLEDGMENTS

This work has been partially supported by the Ministerio de Ciencia e Innovación under Project No. TEC2009-06986 and by the DURSI of the Generalitat de Catalunya under Contract No. 2009SGR783. J. Suñé acknowledges support from ICREA ACADEMIA.

APPENDIX A: QUALITATIVE ESTIMATION OF LEAD RESISTANCE IN PURE BALLISTIC DEVICES

As mentioned in the introduction, the importance of the resistance in the leads when dealing with electric transport through ballistic devices was well understood some time ago due to the enlightening work of Landauer, Büttiker, and co-workers¹⁻⁵ on the “two-terminal” G^{2t} and “four-terminal” G^{4t} conductances. We will use here an argument to obtain the same lead resistances but emphasizing the role of the overall charge neutrality requirement mentioned along this paper. The effect of these lead resistances on the measured characteristics of the electron device is, somehow, rediscovered for

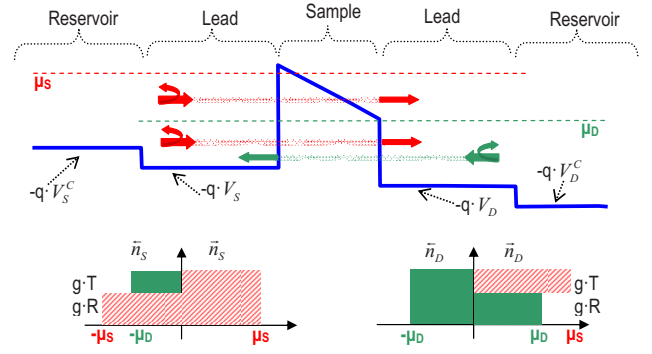


FIG. 18. (Color online) Schematic representation of the bottom of the conduction band and the electrochemical potential as a function of position for a tunneling obstacle with transmission T and reflection R coefficients. Left/right insets: particle density on the source/drain lead as a function of the kinetic energy (with sign defined by their velocity direction) of electrons. The total particle density $\tilde{n}_{S/D}$ ($\tilde{n}_{S/D}$) of electrons in the source/drain lead is equal to the area above of the negative (positive) axis. Solid green (dashed red) indicates electrons initially injected from the drain (source) reservoir.

each new generation of electron-transport simulator (see, for example, Ref. 33 for a discussion of this issue on the self-consistent scattering-states algorithm for a RTD or Ref. 45 for a DFT electron-transport simulator).

As depicted in Fig. 18, we define the sample (or the active region⁶) as an obstacle that is tunneled by electrons. We do also consider two ideal reservoirs acting as a perfect (absorbing/emitting) black bodies with a source μ_S and drain μ_D well-defined electrochemical potentials. We defined the leads as the region that connects the obstacle (i.e., sample) with the ideal reservoirs. Electrons leaving the sample, either by transmission or reflection, are effectively screened and they suffer inelastic scattering, so that their energy distribution becomes a (quasi-) equilibrium distribution at the reservoir. The “two terminals” conductance $G^{2t} = I/V^{2t} = 2q^2T/h$ is defined as the total average (dc) current I divided by the voltage drop $V^{2t} = V_D^C - V_S^C$ between the reservoirs.¹⁻³ The parameter T is the transmission coefficient of a tunneling obstacle, h the Plank constant. The original formulation of the “four terminals” conductance proposed by Landauer^{4,5} was $G^{4t} = I/V^{4t} = 2q^2/h(T/R)$, when $V^{4t} = V_D - V_S$. The difference between both expressions is due to the resistance (i.e., voltage drop) in the leads.

Now, we deduce the value of such lead resistances in the source and drain by imposing (a simplified version of) the overall charge neutrality requirement mentioned in the paper. As seen in Fig. 18, we apply a bias $V^{2t} = V_D^C - V_S^C = (\mu_S - \mu_D)/q$ with net flux of electrons from source to drain. The energies $-qV_S^C$ and $-qV_D^C$ are the conduction band bottom at the source and drain reservoir, respectively. Deep inside the source reservoirs, the total particle density is equal to the doping density N_D . Thus, $n_S^C = \tilde{n}_S^C + \tilde{n}_S^C = N_D$, where \tilde{n}_S^C and \tilde{n}_S^C refer to the particle density of electrons with positive (from left to right) and negative velocities, respectively. If the series resistances of the reservoirs are negligible, we can assume $\tilde{n}_S^C = g(\mu_S + qV_S^C) = N_D/2$ and $\tilde{n}_S^C = g(\mu_S + qV_S^C) = N_D/2$

where g is the density of states that we assume constant in order to avoid irrelevant energy integrals in our *qualitative* argumentation. In addition, zero temperature is assumed to simplify arguments. Identical charge distribution can be defined in the drain reservoir.

However, close to the barrier, in the leads, the electron charge density depends on the barrier transmittance. The number of electrons arriving at one lead depends on the number of electrons injected from the reservoir of the other side and the transmission of the barrier. For example, electrons with negative velocity in the source lead are those incident from the drain region and effectively transmitted, plus those incident from the source that have been reflected by the barrier, $\tilde{n}_S = Tg(\mu_D + qV_S) + Rg(\mu_S + qV_S)$. On the other hand, electrons with positive velocity in the source lead are $\tilde{n}_S = g(\mu_S + qV_S)$. In particular, in a simple treatment of the Coulomb interaction, we define $-qV_S$ and $-qV_D$ as the energies of the conduction band bottom at the source and drain leads, respectively. See left inset in source region of Fig. 18.

In order to accomplish the overall-charge-neutrality condition, assuming that the reservoirs are already neutral and that the charge in the barrier regions is negligible, then, the total charge in each lead must be neutral (i.e., electron charge equal to the doping) to assure overall charge neutrality in the whole device. This is the crucial point of our argumentation in this appendix. Therefore, for the degenerate system considered here (where the Pauli principle implies that any increase in charge must come from higher energies) the voltage close to the barrier must vary to accommodate the previous charge-neutrality restriction. Thus, the charge neutrality at the leads, $\tilde{n}_S + \tilde{n}_S = N_D$ with $\tilde{n}_S = Tg(\mu_D + qV_S) + Rg(\mu_S + qV_S)$ and $\tilde{n}_S = g(\mu_S + qV_S)$, implies the following relationship between the reservoir and lead voltages, $V_S = V_S^C + T(\mu_S - \mu_D)/(2q)$, with a source lead “pseudoresistance” equal to

$$R_{SL} = \frac{V_S - V_S^C}{I} = \frac{T(\mu_S - \mu_D)/(2q)}{2q^2 T/hV^{2t}} = \frac{1}{2} \frac{h}{2q^2}. \quad (\text{A1})$$

The bottom of the conduction band decreases in the source lead because the number of electrons with negative velocity is less than expected in the energy range $\mu_S - \mu_D$ (i.e., only electrons reflected by the barrier in the source will contribute to \tilde{n}_S). Identically, electrons with positive velocity in the drain lead are transmitted electrons from the source or reflected electrons from the drain, $\tilde{n}_D = Tg(\mu_S + qV_D) + Rg(\mu_D + qV_D)$ and $\tilde{n}_D = g(\mu_D + qV_D)$. Then, from the charge neutrality condition, $\tilde{n}_D + \tilde{n}_D = N_D$, we obtain the relation $V_D = V_D^C - T(\mu_S - \mu_D)/(2 \cdot q)$ that implies the drain lead pseudoresistance

$$R_{DL} = \frac{V_D^C - V_D}{I} = \frac{T(\mu_S - \mu_D)/(2q)}{2q^2 T/hV^{2t}} = \frac{1}{2} \frac{h}{2q^2}. \quad (\text{A2})$$

Again, we realize that the bottom of the conduction band in the drain lead have to be a bit higher than that deep in the reservoir because the number of electrons with positive velocity is more than expected in the energy range $\mu_S - \mu_D$.

In many textbooks,⁶⁵ there is an even simpler development of the expression of the source in Eq. (A1) and drain in Eq. (A2) lead expressions of the pseudoresistances. If we

assume a zero-series resistance in the reservoir, the total conductance $G^{2t} = I/V^{2t} = 2q^2 T/h$ can be decomposed as follows:

$$\begin{aligned} \frac{1}{G^{2t}} &= \frac{h}{2q^2 T} = \frac{h}{2q^2} \left(1 + \frac{1-T}{T} \right) = \frac{h}{2q^2} + \frac{h}{2q^2} \frac{R}{T} \\ &= R_{SL} + R_{DL} + \frac{h}{2q^2} \frac{R}{T}, \end{aligned} \quad (\text{A3})$$

where $R_{SL} = h/4q^2$ is the source lead resistance, $R_{DL} = h/4q^2$ is the drain lead resistance and $hR/(2q^2 T)$ the intrinsic sample resistance deduced by Landauer, originally.

This simple example does show the inevitable presence of lead resistances in ballistic systems. The accurate computation of such resistances needs a more appropriate treatment of the Coulomb interaction among electrons than the capacitive linear relation between charge and voltage that we have assumed above. Therefore, a better treatment of coulomb interaction in the leads needs a self-consistent solution of the charge density and scalar potential, as we did in the paper.

Finally, let us emphasize the different origins of the standard-series resistance present in any electron device and the lead resistances discussed here. The former is due to the presence of a small and homogenous electric field deep inside the reservoir, which provides a net current. The voltage drop in the reservoir is only due to this homogenous electric field deep inside the reservoir where local charge neutrality is guaranteed. However, the voltage drop in the leads is imposed by the Poisson (Gauss) equation that relates the shape of the charge density to the voltage drop in the conduction band close to the tunneling obstacle with a complicated non-homogenous electric field. As seen in Sec. II B, the first term of the right-hand side of expressions (21) and (22) account for the reservoir series resistance while the rest account for the complicated lead resistance.

APPENDIX B: THE QUASISTATIC ELECTROMAGNETIC APPROXIMATION FOR THE TIME-DEPENDENT SIMULATION OF NANOSCALE ELECTRON DEVICES

Along this paper, we have assumed that the dynamics of electrons is controlled only by the scalar potential. We have argued that our algorithm is valid even for terahertz frequencies. However, in principle, any time-dependent variation in the scalar potential must imply a time-dependent vector potential. We discuss here the validity of our assumption of neglecting the vector potential.

In principle, electron dynamics in nanoscale electron devices are determined by, both, the (time-dependent) electric field intensity, $\vec{E}(\vec{r}, t)$, and the magnetic flux density, $\vec{B}(\vec{r}, t)$. The electric field intensity is computed from the scalar potential, $V(\vec{r}, t)$, and the vector potential, $\vec{A}(\vec{r}, t)$

$$\vec{E}(\vec{r}, t) = -\vec{\nabla}V(\vec{r}, t) - \frac{\partial \vec{A}(\vec{r}, t)}{\partial t} \quad (\text{B1})$$

while $\vec{B}(\vec{r}, t)$ depends only on the vector potential $\vec{B}(\vec{r}, t) = \vec{\nabla} \times \vec{A}(\vec{r}, t)$. These electromagnetic fields can be computed from the four well-known Maxwell¹⁷ equations

$$\vec{\nabla} \cdot \vec{D}(\vec{r}, t) = \rho(\vec{r}, t), \quad (\text{B2a})$$

$$\vec{\nabla} \cdot \vec{B}(\vec{r}, t) = 0, \quad (\text{B2b})$$

$$\vec{\nabla} \wedge \vec{E}(\vec{r}, t) = -\frac{\partial \vec{B}(\vec{r}, t)}{\partial t}, \quad (\text{B2c})$$

$$\vec{\nabla} \wedge \vec{H}(\vec{r}, t) = \vec{J}(\vec{r}, t) + \frac{\partial \vec{D}(\vec{r}, t)}{\partial t}, \quad (\text{B2d})$$

where $\vec{H}(\vec{r}, t) = \vec{B}(\vec{r}, t)/\mu$ and $\vec{D}(\vec{r}, t) = \epsilon \vec{E}(\vec{r}, t)$ are the magnetic and electric flux intensities, and $\vec{J}_c(\vec{r}, t)$ and $\rho(\vec{r}, t)$ are the (particle) current and charge densities, respectively.

However, when no external magnetic field is applied to a nanoscale electron device, the electron dynamic in nanoscale systems can be computed only from the scalar potential. This quasistatic electromagnetic approximation assumes that the time-dependent magnetic induction in the definition of the electric field in Eq. (B2c) can be neglected. Then, the electric field is essentially an irrotational vector, $\vec{\nabla} \wedge \vec{E}(\vec{r}, t) = 0$. Therefore, the electric field, decoupled from the magnetic counterpart, can be computed from

$$\vec{E}(\vec{r}, t) \approx -\vec{\nabla} V(\vec{r}, t). \quad (\text{B3})$$

Equations (B3) leads to the time-dependent Poisson equation used in our paper

$$\vec{\nabla}[\epsilon \vec{\nabla} V(\vec{r}, t)] = -\rho(\vec{r}, t). \quad (\text{B4})$$

The (time-dependent) boundaries conditions of the scalar potential imposed on the open⁵² borders of the simulation box are the central issue of this paper.

Let us discuss the limits of applicability of the quasistatic approximation in nanoscale electron devices. For a simple estimations, we assume only one typical length scale L so that we can approximate spatial derivatives that make up the curl and divergence operators by $\partial/\partial x \sim 1/L$. Identically, we assume that time derivatives are roughly equal to a multiplying factor f related to the frequency of the signal, $\partial/\partial t \sim f$. Then, from the gauss law in Eq. (B1) we obtain for the

charge density $\rho(\vec{r}, t) \approx \epsilon \cdot E/L$ with $E \equiv \max|\vec{E}(\vec{r}, t)|$. Identically, from the continuity equation

$$\frac{\partial \rho(\vec{r}, t)}{\partial t} + \vec{\nabla} \cdot \vec{J}(\vec{r}, t) = 0, \quad (\text{B5})$$

we obtain for the current density $\vec{J}(\vec{r}, t) \approx \epsilon \cdot E \cdot f$. From the knowledge of the current and charge density, we can estimate the magnetic flux, using Eq. (B1), as $\vec{B}(\vec{r}, t) \approx \mu \cdot \epsilon \cdot f L E$ (we neglect numerical factors such as 2). Then, the vector potential is $\vec{A}(\vec{r}, t) \approx \mu \cdot \epsilon \cdot f L^2 E$ and its time derivative is $\partial \vec{A}(\vec{r}, t)/\partial t \approx \mu \cdot \epsilon \cdot f^2 L^2 E$. On the other hand, the gradient of the scalar potential can be written as $\vec{\nabla} V(\vec{r}, t) \approx E$. Finally, we obtain that the electric field in Eq. (B1) can be written as expression (B3) under the quasistatic assumption $\mu \cdot \epsilon \cdot f^2 L^2 \ll 1$. This inequality can be interpreted as the condition that the length L of the system is much smaller than the wavelength $\lambda = c/f$ of the electromagnetic signal of frequency f (with $c = 1/\sqrt{\mu \epsilon}$ the speed of the electromagnetic signal). For the dimensions used in this work, never longer than few hundreds of nanometers, the contribution of the electromagnetic vector potential can be reasonably neglected at frequencies lower than about 10 THz.^{66,67} If one is interested in using larger reservoirs (with L on the order of microns) this approximation is not valid and a whole electromagnetic solution is needed to treat electromagnetic transport, as discussed in Ref. 68.

Let us clarify that one can arrive to the time-dependent Poisson Eq. (B4) directly from the Coulomb gauge. We have not followed this path here because we are not only interested in arriving to Eq. (B4) but also in showing that the electric field is much more important than the magnetic field when describing electron dynamics. In particular, with the approximations discussed above we realize that the Lorentz force $\vec{F}(\vec{r}, t) = q \cdot \vec{E}(\vec{r}, t) + q \cdot \vec{v}(\vec{r}, t) \times \vec{B}(\vec{r}, t)$ can be written as $|\vec{F}(\vec{r}, t)| \approx q \cdot E + q \mu \cdot \epsilon \cdot f^2 L^2 E$, where we have assumed that the electron velocity $|\vec{v}(\vec{r}, t)| \leq Lf$. Then, from the previous scenarios that satisfy the quasistatic condition $\mu \cdot \epsilon \cdot f^2 L^2 \ll 1$, we realize identically that the magnetic field can be neglected in front of the electric field when describing electron dynamics.

*xavier.oriols@uab.es

¹Y. M. Blanter and M. Büttiker, *Phys. Rep.* **336**, 2 (2000).

²R. Landauer, *Phys. Scr.* **T42**, 110 (1992).

³M. Büttiker, Y. Imry, R. Landauer, and S. Pinhas, *Phys. Rev. B* **31**, 6207 (1985).

⁴R. Landauer, *Philos. Mag.* **21**, 863 (1970).

⁵R. Landauer, *IBM J. Res. Dev.* **1**, 223 (1957).

⁶In this paper, we refer to the “sample” as the device active region and the “leads” as the regions connecting the sample and the ideal (black-body) reservoirs. The reservoirs are usually called “contacts” in mesoscopic devices. We avoid this last name here because, in those papers related with the simulation of atomistic

structures, the word contacts are usually understood as what we call here the sample.

⁷M. Büttiker, H. Thomas, and A. Prêtre, *Phys. Lett. A* **180**, 364 (1993).

⁸M. Büttiker, A. Prêtre, and H. Thomas, *Phys. Rev. Lett.* **70**, 4114 (1993).

⁹M. Büttiker, H. Thomas and A. Prêtre, *Z. Phys. B* **94**, 133 (1994).

¹⁰M. Büttiker, *J. Phys.: Condens. Matter* **5**, 9361 (1993).

¹¹M. Büttiker and S. E. Nigg, *Nanotechnology* **18**, 044029 (2007).

¹²M. C. Goorden and M. Büttiker, *Phys. Rev. Lett.* **99**, 146801 (2007).

- ¹³In principle, a formal quantum treatment of the openness of the sample requires quite elaborate formalisms to “trace out” the degrees of freedom not explicitly simulated (Ref. 68). In this sense, the Lindblad (Ref. 69) or quantum master equations are the accurate substitutes of the Schrödinger or Liouville equations which are applicable for closed systems. This formal treatment of an open system is far from the scope of this work and we follow the standard way of dealing with open systems by specifying educated guesses for the BCs on the borders of the simulation box.
- ¹⁴J. Taylor, H. Guo, and J. Wang, *Phys. Rev. B* **63**, 245407 (2001).
- ¹⁵M. Brandbyge, J. L. Mozos, P. Ordejón, J. Taylor, and K. Stokbro, *Phys. Rev. B* **65**, 165401 (2002).
- ¹⁶J. P. Colinge, C.-W. Lee, A. Afzaljan, N. D. Akhavan, R. Yan, I. Ferain, P. Razavi, B. O’Neill, A. Blake, M. White, A.-M. Kellerher, B. McCarthy, and R. Murphy, *Nat. Nanotechnol.* **5**, 225 (2010).
- ¹⁷M. Javid and P. M. Brown, *Field Analysis and Electromagnetics* (McGraw-Hill, New York, USA, 1963).
- ¹⁸T. Gonzalez and D. Pardo, *Solid-State Electron.* **39**, 555 (1996).
- ¹⁹G. Gomila, I. R. Cantalapiedra, T. Gonzalez, and L. Reggiani, *Phys. Rev. B* **66**, 075302 (2002).
- ²⁰C. Jacoboni and P. Lugli, *The Monte Carlo Method for Semiconductor Device Simulation* (Springer-Verlag, Wien, New York, 1989).
- ²¹R. Ugajin, A. Ishibashi, K. Funato, and Y. Mori, *J. Appl. Phys.* **73**, 1 (1993).
- ²²A. Reklaitis and L. Reggiani, *Phys. Rev. B* **60**, 11683 (1999).
- ²³T. González, O. M. Bulashenko, J. Mateos, D. Pardo, and L. Reggiani, *Phys. Rev. B* **56**, 6424 (1997).
- ²⁴O. M. Bulashenko, J. Mateos, D. Pardo, T. Gonzalez, L. Reggiani, and J. M. Rubí, *Phys. Rev. B* **57**, 1366 (1998).
- ²⁵M. V. Fischetti and S. E. Laux, *J. Appl. Phys.* **89**, 1205 (2001).
- ²⁶C. J. Wordelman and U. Ravaioli, *IEEE Trans. Electron Devices* **47**, 410 (2000).
- ²⁷S. Babiker, A. Asenov, N. Cameron, and S. P. Beaumont, *IEEE Trans. Electron Devices* **43**, 2032 (1996).
- ²⁸C. Riddet, A. R. Brown, S. Roy, and A. Asenov, *J. Comput. Electron.* **7**, 231 (2008).
- ²⁹D. Reid, C. Millar, G. Roy, S. Roy, and A. Asenov, *IEEE Trans. Electron Devices* **56**, 2255 (2009).
- ³⁰G. Albareda, J. Suñé, and X. Oriols, *Phys. Rev. B* **79**, 075315 (2009).
- ³¹B. Ricco and M. Y. Azbel, *Phys. Rev. B* **29**, 1970 (1984).
- ³²M. O. Vassell, J. Lee, and H. F. Lockwood, *J. Appl. Phys.* **54**, 5206 (1983).
- ³³W. Pötz, *J. Appl. Phys.* **66**, 2458 (1989).
- ³⁴M. J. McLennan, Y. Lee, and S. Datta, *Phys. Rev. B* **43**, 13846 (1991).
- ³⁵A. Rahman, J. Guo, S. Datta, and M. S. Lundstrom, *IEEE Trans. Electron Devices* **50**, 1853 (2003).
- ³⁶R. Venugopal, Z. Ren, and M. S. Lundstrom, *IEEE Trans. Nanotechnol.* **2**, 135 (2003).
- ³⁷Z. Ren, R. Venugopal, S. Goasguen, S. Datta, and M. S. Lundstrom, *IEEE Trans. Electron Devices* **50**, 1914 (2003).
- ³⁸R. Venugopal, S. Goasguen, S. Datta, and M. S. Lundstrom, *J. Appl. Phys.* **95**, 292 (2004).
- ³⁹G. C. Liang, A. W. Ghosh, M. Paulsson, and S. Datta, *Phys. Rev. B* **69**, 115302 (2004).
- ⁴⁰J. Gabelli, G. Fève, J.-M. Berroir, B. Plaçais, A. Cavanna, B. Etienne, Y. Jin, and D. C. Glatli, *Science* **313**, 499 (2006).
- ⁴¹T. C. Au Yeung, Y. Yu, W. Z. Shangguan, and W. K. Chow, *Phys. Rev. B* **68**, 075316 (2003).
- ⁴²J. Quan, Y. Yu, and Y. H. Tang, *Phys. Rev. B* **73**, 195314 (2006).
- ⁴³N. D. Lang, *Phys. Rev. B* **52**, 5335 (1995).
- ⁴⁴M. Di Ventra, S. T. Pantelides, and N. D. Lang, *Phys. Rev. Lett.* **84**, 979 (2000).
- ⁴⁵M. Di Ventra and N. D. Lang, *Phys. Rev. B* **65**, 045402 (2001).
- ⁴⁶R. Baer, T. Seideman, S. Llani, and D. Neuhauser, *J. Chem. Phys.* **120**, 3387 (2004).
- ⁴⁷X. Q. Li and Y. J. Yan, *Phys. Rev. B* **75**, 075114 (2007).
- ⁴⁸S. Kurth, G. Stefanucci, C. O. Almbladh, A. Rubio, and E. K. U. Gross, *Phys. Rev. B* **72**, 035308 (2005).
- ⁴⁹R. Baer and D. Neuhauser, *Int. J. Quantum Chem.* **91**, 524 (2003).
- ⁵⁰X. Oriols, *Phys. Rev. Lett.* **98**, 066803 (2007).
- ⁵¹Thomas Ihn, *Semiconductor Nanostructures: Quantum States and Electronic Transport* (Oxford University Press, New York, 2010).
- ⁵²Due to the openness of the system, we can distinguish between open borders that allow the flux of particles and “close” borders that do not. In this work, we discuss only the modeling of the BCs of such open borders.
- ⁵³X. Oriols, J. Suñé, F. Martín, and X. Aymerich, *J. Appl. Phys.* **78**, 2135 (1995).
- ⁵⁴G. F. Giuliani and G. E. Simion, *Solid State Commun.* **127**, 789 (2003).
- ⁵⁵V. A. Sablikov, S. V. Polyakov, and M. Büttiker, *Phys. Rev. B* **61**, 13763 (2000).
- ⁵⁶X. Oriols, E. Fernandez-Diaz, A. Alvarez, and A. Alarcon, *Solid-State Electron.* **51**, 306 (2007).
- ⁵⁷See an alternative demonstration to the periodic (Born-Von-Karman) Boundary conditions in reference: X. Oriols, *Nanotechnology* **15**, 167(S) (2004).
- ⁵⁸M. Büttiker, *Phys. Rev. Lett.* **65**, 2901 (1990).
- ⁵⁹L. S. Levitov and G. B. Lesovik, *JETP Lett.* **58**, 230 (1993).
- ⁶⁰Strictly speaking, our many-electron method applied to semiclassical devices cannot be considered as a direct solution of the Boltzmann equation because the latter is developed within a classical mean-field approximation. In the approach explained in Ref. 30, each particle “sees” its own electrostatic potential (or electric field), which is different from that of others. This is the fundamental difference between our many-electron method applied to classical transport and the standard MC method for electron transport. See Ref. 30 for a detailed explanation.
- ⁶¹J. Wang, A. Rahman, A. Ghosh, G. Klimeck, and M. Lundstrom, *IEEE Trans. Electron Devices* **52**, 1589 (2005).
- ⁶²M. Born and R. Oppenheimer, *Ann. Phys.* **84**, 0457 (1927).
- ⁶³V. Sverdlov, X. Oriols, and K. Likharev, *IEEE Trans. Nanotechnol.* **2**, 59 (2003).
- ⁶⁴C. Jacoboni and L. Reggiani, *Rev. Mod. Phys.* **55**, 645 (1983).
- ⁶⁵S. Datta, *Electronic Transport in Mesoscopic Systems* (Cambridge University Press, Cambridge, 1995).
- ⁶⁶B. Pellegrini, *Phys. Rev. B* **34**, 5921 (1986).
- ⁶⁷B. Pellegrini, *Nuovo Cimento D* **15**, 855 (1993).
- ⁶⁸M. Di Ventra, *Electric Transport in Nanoscale Systems* (Cambridge University Press, Cambridge, 2008).
- ⁶⁹G. Lindblad, *Commun. Math. Phys.* **48**, 119 (1976).